

THE PANCHROMATIC VIEW OF THE MAGELLANIC CLOUDS FROM CLASSICAL CEPHEIDS. I. DISTANCE, REDDENING AND GEOMETRY OF THE LARGE MAGELLANIC CLOUD DISK

L. INNO^{1,2}, G. BONO^{3,2}, N. MATSUNAGA⁴, G. FIORENTINO⁵, M. MARCONI⁶, B. LEMASLE⁷, R. DA SILVA^{2,3,8}, I. SOSZYŃSKI⁹,
A. UDALSKI⁹, M. ROMANIELLO^{10,11} AND H.-W. RIX¹

Draft version November 6, 2018

ABSTRACT

We present a detailed investigation of the Large Magellanic Cloud (LMC) disk using classical Cepheids. Our analysis is based on optical (I,V ; OGLE-IV), near-infrared (NIR: J,H,K_S) and mid-infrared (MIR: $w1$; WISE) mean magnitudes. By adopting new templates to estimate the NIR mean magnitudes from single-epoch measurements, we build the currently most accurate, largest and homogeneous multi-band dataset of LMC Cepheids. We determine Cepheid individual distances using optical and NIR Period-Wesenheit relations (PWRs), to measure the geometry of the LMC disk and its viewing angles. Cepheid distances based on optical PWRs are precise at 3%, but accurate to 7%, while the ones based on NIR PWRs are more accurate (to 3%), but less precise (2%–15%), given the higher photometric error on the observed magnitudes. We found an inclination $i=25.05 \pm 0.02$ (stat.) ± 0.55 (syst.) deg, and a position angle of the lines of nodes P.A.= 150.76 ± 0.02 (stat.) ± 0.07 (syst.) deg. These values agree well with estimates based either on young (Red Supergiants) or on intermediate-age (Asymptotic Giant Branch, Red Clump) stellar tracers, but they significantly differ from evaluations based on old (RR Lyrae) stellar tracers. This indicates that young/intermediate and old stellar populations have different spatial distributions. Finally, by using the reddening-law fitting approach, we provide a reddening map of the LMC disk which is ten times more accurate and two times larger than similar maps in the literature. We also found an LMC true distance modulus of $\mu_{0,LMC} = 18.48 \pm 0.10$ (stat. and syst.) mag, in excellent agreement with the currently most accurate measurement (Pietrzyński et al. 2013).

Subject headings: Magellanic Clouds — stars: variables: Cepheids — stars: distances — stars: oscillations

1. INTRODUCTION

The Large and Small Magellanic Clouds (LMC and SMC) represent a unique example of star-forming, dwarf interacting galaxies in the Local Group. Moreover, the Magellanic Clouds (MCs) system is embedded in the Milky Way gravitational potential, thus their dynamical history strongly affects the evolution of our own Galaxy. Yet, we still lack a comprehensive understanding of the dynamical history of the complex system MCs-Milky Way. From the theoretical point of view, two scenarios have emerged: the first-infall (unbound) scenario (Besla et al. 2007, 2016), and the multiple-passage (bound) sce-

nario (Diaz & Bekki 2011). In the former, the MCs have been interacting between each other for most of the Hubble time, also experiencing at least one close encounter (~ 500 Myr ago), while they are just past their first pericentric passage. In the more classical bound scenario, the Milky Way potential determines the orbits of the MCs, that formed as independent satellites and only recently (~ 2 Gyr ago) become a binary system of galaxies (see D’Onghia & Fox 2015, for a thorough review).

Even though it has proved to be challenging to distinguish between the two scenarios on the basis of observational constraints, evidence is mounting that the Clouds are now approaching the Milky Way for the first time (Besla et al. 2016). In particular, detailed three-dimensional study of the LMC kinematics obtained from the Hubble Space Telescope shows that the relative orientation of the velocity vectors implies at least one close encounter in the past 500 Myr (Kallivayalil et al. 2013). This is further supported by the distribution of OB stars in the Clouds and the Bridge (a stream of neutral hydrogen that connects the MCs, Mathewson et al. 1974), which suggests a recent (~ 200 Myr ago) exchange of material (Casetti-Dinescu et al. 2014). In this context, the irregular morphology of the Clouds is shaped by their reciprocal interaction. Recent dynamical simulations (Besla et al. 2016, 2012; Diaz & Bekki 2012) show that the off-centre, warped stellar bar of the LMC, and its one-armed spiral naturally arise from a direct collision with the SMC. Thus, the observed morphology of the LMC can be directly related to its dynamical history.

¹ Max-Planck-Institut für Astronomy, 69117, Heidelberg, Germany, inno@mpia.de

² INAF-OAR, via Frascati 33, Monte Porzio Catone, Rome, Italy

³ Dipartimento di Fisica, Università di Roma Tor Vergata, via della Ricerca Scientifica 1, 00133 Rome, Italy

⁴ Department of Astronomy, The University of Tokyo, 7-3-1 Hongo, Bunkyo-ku, Tokyo 113-0033, Japan

⁵ INAF-Osservatorio Astronomico di Bologna, via Ranzani 1, I-40127 Bologna, Italy;

⁶ INAF-Osservatorio Astronomico di Capodimonte, via Moiarello 16, 80131 Napoli, Italy

⁷ Anton Pannekoek Astronomical Institute, Science Park 904, P.O. Box 94249, 1090 GE Amsterdam, The Netherlands

⁸ ASI Science Data Center, ASDC c/o ESRIN, via del Politecnico snc, 00133 Rome, Italy

⁹ Warsaw University Observatory, Al. Ujazdowskie 4, 00-478 Warszawa, Poland

¹⁰ European Southern Observatory, Karl-Schwarzschild-Str. 2, 85748 Garching bei Munchen, Germany

¹¹ Excellence Cluster Universe, Boltzmannstr. 2, D-85748, Garching, Germany

This is the first paper of a series aimed at investigating the morphology, the kinematics and the chemical abundances of the Large and Small Magellanic Clouds by adopting Classical Cepheids as tracers of the young stellar populations in these galaxies. In the current investigation, we focus our attention on the LMC geometry and three-dimensional structure, by using Cepheids optical (V, I) and near-infrared (NIR, J, H and K_S) period-luminosity (PL) and period-Wesenheit (PW) relations.

The LMC viewing angles, the inclination i and the position angle P.A. of the lines of nodes (the intersection of the galaxy plane and the sky plane), are basic parameters that describe the directions towards which we observe the LMC disk. The determination of such angles has major implications on the the determination of the dynamical state of the Milky-Way–MCs system. For instance, the uncertainty on the determinations on these angles affects the quoted results on the LMC kinematics, because they are needed to transform the line-of-sight velocities and proper motions into circular velocities, and, in turn, to determine the orbits of the stars. The LMC viewing angle estimates available in the literature span a wide range of values.

It is somehow expected that different stellar tracers and methods will provide different results because *a*) the old and young stellar populations in the LMC show different geometrical distributions (de Vaucouleurs & Freeman 1972; van der Marel & Cioni 2001; Cioni et al. 2000; Weinberg & Nikolaev 2001), and *b*) these distributions are non-axisymmetric, so results also depend on the fraction of the galaxy covered by the adopted tracer.

Viewing angles based on studies of Red Giants (RG, $i = 34^\circ.7 \pm 6^\circ.2$, P.A. = $122^\circ.5 \pm 8.3^\circ$, van der Marel & Cioni 2001) are consistent with the values found on the basis of RR Lyrae variable stars from the OGLE-III catalog ($i = 32^\circ.4 \pm 4^\circ$, P.A. = $115^\circ \pm 15^\circ$, Haschke et al. 2012). New estimates only based on ab-type of RR Lyrae stars ($i = 22^\circ.25 \pm 0^\circ.01$, P.A. = $175^\circ.22 \pm 0^\circ.01$, Deb & Singh 2014), do not support previous findings based on the same tracers, but they agree with the values based on HI kinematics (Kim et al. 1998). The quoted uncertainties and the limited precision in dating individual Red Clump (RC) stars do not allow us to single out whether old and intermediate-age stellar tracers display different spatial distributions ($i = 26^\circ.6 \pm 1^\circ.3$, P.A. = $148^\circ.3 \pm 3.8^\circ$, Subramanian & Subramanian 2013). Moreover, LMC viewing angles based on stellar tracers younger than $\lesssim 600$ Myr display conflicting values. Using optical (from MACHO, Alcock et al. 2000) and NIR (from DENIS, Epchtein 1998) data for $\sim 2,000$ Cepheids, Nikolaev et al. (2004) found a position angle of P.A. = $150^\circ.2 \pm 2^\circ.4$ and an inclination of $i = 31^\circ \pm 1^\circ$.

On the other hand, Rubele et al. (2012) using NIR measurements from the Vista Survey for the Magellanic Clouds (VMC, Cioni et al. 2011) found a smaller position angle, P.A. = $129^\circ.2 \pm 13^\circ$, and a smaller inclination, $i = 26^\circ.2 \pm 2^\circ$. Interestingly enough, the position angle found by Nikolaev et al. (2004) agrees quite well with the value estimated by van der Marel & Kallivayalil (2014) using the kinematics of young stars ($\lesssim 50$ Myr). More recently, Jacyszyn-Dobrzyniecka et al. (2016) used optical mean magnitudes for Cepheids from the OGLE-IV Collection of Classical Cepheids (CCs, Soszyński et al. 2015, hereinafter S15), including more than 4,600 LMC

Cepheids. They found a smaller inclination ($i = 24^\circ.2 \pm 0^\circ.6$) and a larger position angle (P.A. = $151^\circ.4 \pm 1^\circ.5$) when compared with Nikolaev et al. (2004).

The large spread of the values summarised above shows how complex it is to estimate the LMC viewing angles, and how difficult it is to correctly estimate both the statistical and the systematic error associated to the measurements.

In this paper we provide a new estimate of the LMC viewing angles, taking advantage of the opportunity to complement the large sample of LMC Cepheids recently released by the OGLE-IV survey, with NIR observations. In particular, we rely on single-epoch observations from the IRSF/SIRIUS (Kato et al. 2007) survey and the 2MASS (Skrutskie et al. 2006), transformed into accurate NIR mean-magnitudes by adopting the new NIR templates by Inno et al. (2015, hereinafter I15). We also provide new mid-infrared (MIR) mean magnitudes from light-curves collected by the ALLWISE- Multi-epoch-catalog (Wide-field Infrared Survey Explorer, Cutri et al. 2013). The complete photometric data-set is presented in Section 2. In Section 3 we derive Cepheid individual distances with an unprecedented precision (0.5% from optical bands, 0.5–15% from NIR bands) and accuracy (7% from optical bands, 3% from NIR bands). We then use the Cepheid individual distances to derive the LMC viewing angles by using geometrical methods described in Section 4. Results are presented in Section 5, and discussed in Section 6. The use of multi-wavelengths magnitudes also allow us to compute the most accurate and extended reddening map towards the LMC disk available to date. A description of the method and the map can be found in Section 7. Moreover, we use the Cepheids' individual reddening to compute new period-luminosity relations corrected for extinction. The summary of the main results of this investigation and an outline of the future developments of this project are given in Section 8.

2. DATA SETS

We adopted the largest dataset of NIR (J, H, K_S) mean magnitudes ever collected for Cepheids in the LMC, that covers $\sim 95\%$ of the recently released new OGLE-IV collection of Classical Cepheids (S15). We define this dataset our Sample A and the the distribution onto the plane of the sky of Cepheids in this sample is shown in Figure 1. Moreover, we cross-matched the LMC Cepheid catalog with the ALLWISE-Mep catalog, in order to complement our data with mid-infrared (MIR, $[3.4] \mu\text{m}$) time-series data. We define our Sample B the dataset that includes only Cepheids for which we have optical, NIR and MIR mean magnitudes.

In particular, our final catalogs includes the following sub-samples:

i) multi-epochs observations for Cepheids from the VMC survey (VMC)

We include the Cepheids for which the first public data release (DR1) of the VMC provided NIR magnitudes measured at five different epochs in the J band and at twelve epochs in the K_S band for 157 Fundamental mode (FU) Cepheids and 135 First Overtone (FO) Cepheids (LMC6_6 tile, see also Ripepi et al. 2012). We adopted the templates by I15 and the period estimates available from the OGLE-IV CCs to perform a template fitting to

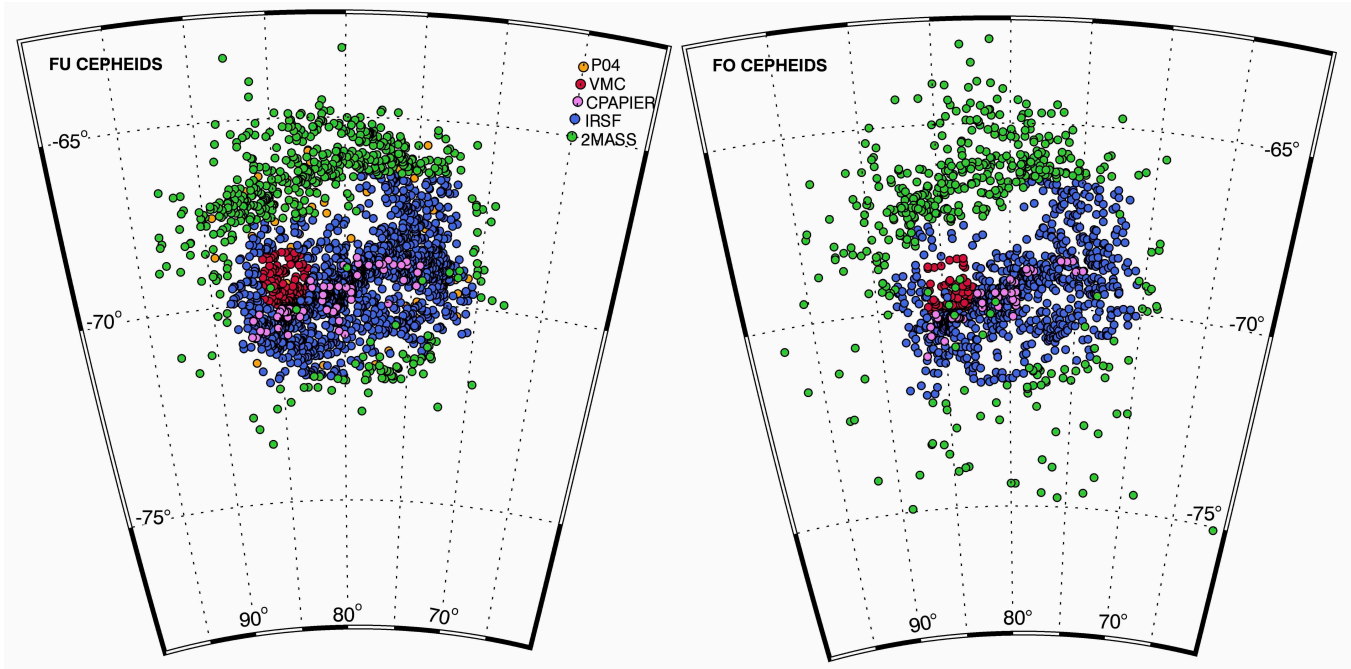


FIG. 1.— Left: Sky distribution of the Fundamental Cepheids (FU) in our optical-NIR sample (Sample A). Different colors indicates the different subsamples: P04 (orange dots), VMC (red dots), CPAPIER (magenta dots), IRSF (blue dots) and 2MASS (dark cyan dots). Right: same as in the left panel but for First-Overtone (FO) Cepheids. A detailed description of the number of Cepheids included in each sub-sample can be found in Table 1. Our total sample (FU+FO), which covers the entire LMC disk and the central bar, is the most accurate, largest and homogeneous multi-band dataset of LMC Cepheids available to date.

the multi-epoch observations in order to determine their mean magnitudes. We independently solved for the light-curve amplitudes, mean magnitudes and phase-lags between the V and the NIR light curves. Figure 2 shows the result of the template fitting for four different Cepheids in the sample, in the case of the K_S -band (top panels) and the J -band observations. The top panel of Figure 2 compares the result of the template fitting (red dashed line) with a third-order Fourier series fitting (light blue dashed line) for two Cepheids with relatively long ($P \sim 20$ days) and short period ($P \sim 6$ days). To make the difference between the two fits more clear, we also show the residuals in the lower part of the plots. The rms of the residuals, indicated by the dashed lines, show that the data have a smaller dispersion around the template fitting, when compared to the Fourier fitting. Moreover, the bottom panel of the same figure shows that the template fitting is also able to properly recover the shape of the light curve, even from few epochs. Without the template, only a single-sinusoid model could be fitted to the data, but this approach fails in dealing with FU Cepheids, due to their asymmetric light curves (Marconi et al. 2013).

We also adopted template fitting for FO Cepheids in the J -band, as they are available in I15, while we performed a third-order Fourier series fitting to estimate the K_S -band mean magnitude for FO Cepheids. The error on the mean magnitude estimates is given by the standard deviation of the data around the best-fit template. The typical final uncertainty is lower than 0.01 mag. Individual uncertainties on the mean magnitudes for the VMC sample data are plotted as red dots in Figure 3. Note that the VMC magnitudes are already provided in the 2MASS photometric system.

ii) multi-epochs observations for Cepheids from the Large Magellanic Cloud Near-Infrared Synoptic Survey (CPAPIER)

Macri et al. (2015) published J , H , and K_S light curves for 866 FU and 551 FO Cepheids collected by the Large Magellanic Cloud Near-Infrared Synoptic Survey, operated at the 1.5m CTIO telescope with the CPAPIER camera. The mean magnitudes and the individual photometric data, calibrated and transformed into the 2MASS photometric system, are publicly available. In order to improve the accuracy on the mean magnitude determination, we downloaded the photometric data for all the observed Cepheids and performed a template fitting of the FU Cepheids light curves, by adopting the templates by I15 and assuming the periods from the OGLE-IV CCs. To perform the fitting, we adopted the same approach described above for the VMC sample. For light-curves successfully fitted, the error on the mean magnitude is computed again as the standard deviation of the data around the best-fit template. The mean magnitudes obtained by our fit are however very similar to the ones obtained by Macri et al. (2015, see their Table 3), in both cases, in fact, the photometric uncertainties on the individual observations, on average larger than 0.02 mag, is limiting the final accuracy on the mean magnitudes. We obtain an uncertainty on the mean magnitudes of ± 0.03 mag for brighter ($J \approx 14$ mag) and ± 0.05 mag for fainter Cepheids. In the case of the FO Cepheids, we adopted the mean magnitudes and uncertainties obtained by Macri et al. (2015). Individual uncertainties on the mean magnitudes for the CPAPIER sample included in our final sample are plotted as magenta dots in Figure 3.

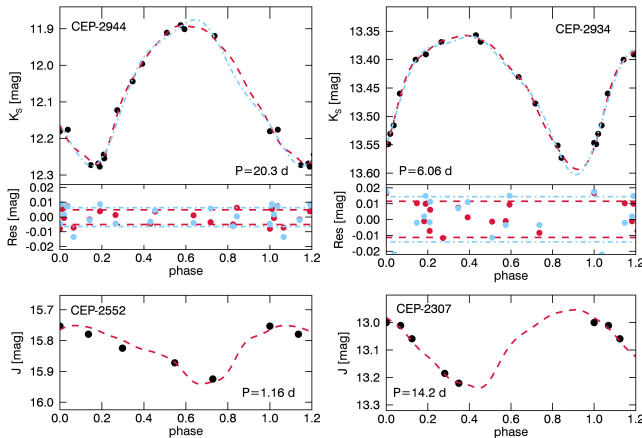


FIG. 2.— Top – Left: Comparison between the VMC observations in the K_S band (black solid dots) and two different light-curve fitting functions: a third order Fourier series (light blue dot-dashed line) and the template fitting by Inno et al. (2015, red dashed line) for the Cepheid OGLE-LMC-CEP-2944. The residuals between the observed data and the fits are also shown in the lower part of the panel as light-blue dots and as red dots respectively. The dashed lines indicate the *rms* of the residual, which is larger for the Fourier fitting. Similar results are shown in the right panel for a different Cepheid: OGLE-LMC-CEP-2934, with a shorter pulsation period. Bottom – Template fitting for the five-epochs J -band observations of Cepheids in the VMC sample for a short period Cepheids (OGLE-LMC-CEP-2552, period ~ 1 day, left panel) and a longer period Cepheid (OGLE-LMC-CEP-2307, period ~ 15 days, left panel). The template fitting correctly recover the shape of the light curves for FU Cepheids over all the period range (1–100 days).

iii) single-epoch observations for Cepheids in the IRSF sample (IRSF)

The IRSF/SIRIUS Survey provided single-epoch measurements in the J , H , and K_S bands for 1627 FU and 1037 FO Cepheids in the LMC. For all these Cepheids, complete V -band light curves are available from the OGLE-IV CCs. Thus, we can apply the prescriptions and the templates by I15 to derive accurate NIR mean magnitudes from the single-epoch observations, by adopting the V -NIR amplitude ratio and the predicted V -NIR phase-lag. The final error on the mean-magnitude is also computed by following the prescriptions given in Section 6.2 of I15. The typical uncertainty on the derived mean magnitudes is ± 0.02 mag for the brighter ($J \approx 12$ mag) and ± 0.05 mag for the fainter Cepheids ($J \approx 17$ mag).

Light-curve templates in the H , and K_S bands for the FO Cepheids are still not available, due to the lack of accurate and well sampled light curves for short-period FO Cepheids. Thus, we can only adopt single-epoch magnitudes as the best approximation of the mean magnitude along the pulsation cycle. Thus, we can only adopt single-epoch magnitudes as the best approximation of the mean luminosity along the pulsation cycle. This approximation introduces an additional uncertainty due to the random phase effect, with an upper limit set by the semi-amplitude of the FO light curves in these two bands. From the CPAPIER data we estimate that the semi-amplitude of LMC FO Cepheids is on average lower than 0.05 mag. Finally, we transformed the mean magnitudes into the 2MASS NIR photometric system following Kato et al. (2007). Individual uncertainties

on the mean magnitudes for the IRSF sample Cepheids are plotted as magenta dots in Figure 3. They typically range from 0.02 to 0.06 mag, when moving from brighter to fainter Cepheids.

iv) single-epoch observations for Cepheids in the 2MASS catalog (2MASS)

We adopted 2MASS single-epoch observations available for all the LMC Cepheids in the OGLE-IV CCs that do not have NIR measurements from any of the other surveys described above. In order to derive the mean magnitudes of these Cepheids, we followed the same approach described above for the IRSF sample. However, because the photometric precision of single-epoch 2MASS data is lower with respect to the IRSF data, the typical uncertainty on the derived mean magnitudes is larger: ± 0.02 mag for the brighter ($J \approx 12$ mag) and ± 0.10 mag for the fainter ($J \approx 17$ mag) Cepheids. Nevertheless, the application of the NIR-templates allow us to improve the accuracy on the mean magnitudes determination, as demonstrated in Figure 4. From the top to the bottom, this Figure shows the distribution of the residuals from Period-Luminosity relations in the J (top), H (middle) and K_S (bottom) bands for the single-epochs 2MASS data (dark green bars) and the single-epochs + templates (lime bars). The distribution is fitted by a Gaussian distribution (over-plotted solid lines) with a dispersion labeled in the left corner of each panel. We find that the use of the templates decreases the residual dispersions of 5%–10%, thus improving the accuracy of the estimate mean magnitudes with respect to the single-epoch observations.

v) mean magnitudes for 66 Cepheids from Persson et al. (2004) (P04)

We completed our NIR sample by including J , H , and K_S mean magnitudes for 66 Cepheids published by Persson et al. (2004, P04) and for which V and I photometric data are also available in the OGLE Catalog. The final accuracy of the NIR mean magnitudes in the P04 catalog is ± 0.02 mag for the brighter ($J \approx 12$) and ± 0.06 mag for the fainter ($J \approx 14$) Cepheids. To transform the NIR measurements from the original LCO photometric system into the 2MASS photometric system, we adopted the relations given by Carpenter (2001). Individual uncertainties on the mean magnitudes for the P04 sample Cepheids are plotted as orange dots in Figure 3.

vi) mean magnitudes for 2,600 Cepheids from ALLWISE- Multi-epochs catalog (WISE)

We complemented our analysis by also including mid-Infrared (MIR) $w1$ mean magnitude from the ALLWISE-Multi-epochs catalog. The data are publicly available and accessible through the IRSA web service¹² The light curves available include from ~ 30 to ~ 200 epochs for each Cepheid in the LMC. We performed a third-order Fourier-series fit to the observed light curve to obtain the flux-averaged mean magnitude in the $w1$ -band (central wavelength $\lambda_c = 3.4 \mu\text{m}$). For light curves with scatter larger than 0.2 mag (~ 100 FU, ~ 200 FU) we adopted the weighted mean of the measurements as the mean magnitude.

¹² <https://irsa.ipac.caltech.edu/cgi-bin/Gator/nph-dd>

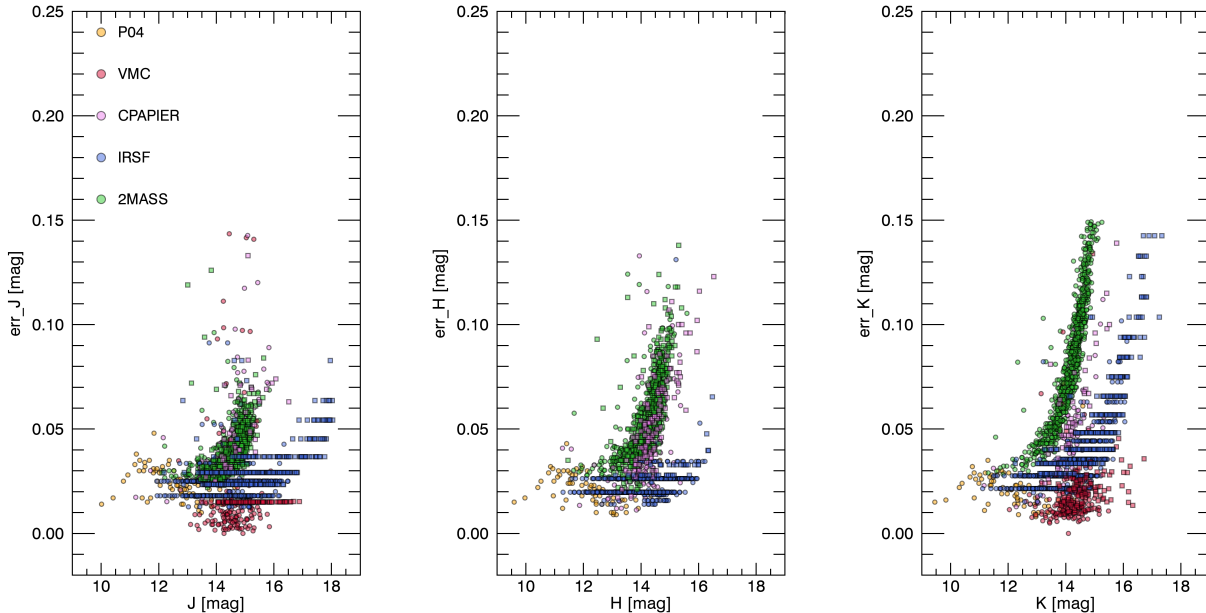


FIG. 3.— Errors on the mean magnitudes as a function of the mean magnitudes in the three different NIR bands: J (left), H (middle) and K_S (right) for FU (dots) and FO (diamonds) Cepheids in our Sample A. The color legend is the same as in the Figure 1: P04 (orange dots), VMC (red dots), CPAPIER (magenta dots), IRSF (blue dots) and 2MASS (dark cyan dots). The VMC and P04 sub-samples are characterised by the best photometric precision, while IRSF and CPAPIER data have larger errors at the faint end. The data from 2MASS are characterised by the lowest photometric precision, with photometric errors ranging from 0.02 mag to 0.15 mag.

2.1. Compilation of the final catalogs

For Cepheids included in different NIR sub-samples, we gave the priority to the data from the P04 sample and then to VMC, IRSF and CPAPIER (H -band) magnitudes. Then we also adopted CPAPIER data for Cepheids with periods longer than 30 days. Finally, 2MASS observations were adopted for Cepheids with no data available from any other NIR catalog.

This means that for FU Cepheids with period shorter than 30 days and FO Cepheids, we preferred the mean magnitudes from the IRSF sample to the ones from the CPAPIER survey. The comparison of the photometric errors for the IRSF and the CPAPIER samples are shown in Figure 3. The data plotted in this Figure indicate that the photometric errors of the former sample is a factor of two smaller than the latter one for almost all the bands. This result can be easily related to the difference in the NIR camera adopted by the two surveys. In fact, both the IRSF and the CPAPIER surveys are carried out at 1.4m telescopes (in South Africa and in Chile, respectively), but the pixel scale of the IRSF/SIRIUS camera ($0.''45 \text{ pixel}^{-1}$) is the half of the CPAPIER one ($0.''98 \text{ pixel}^{-1}$). This means a better spatial resolution, and in turn, more accurate photometry in crowded stellar fields. To provide more quantitative estimates of the difference among different NIR datasets, Figure 5 shows the offset in mean color $J - K_S$ for Cepheids in common among different sub-samples: 23 FU Cepheids with mean colors from the P04 sample plus 81 from the VMC sample, for which we also have mean colors from the CPAPIER and the IRSF surveys. We assume that the mean colors given in the P04 and VMC samples are the *reference* ones, and we compute the difference with the CPAPIER (magenta bars) and the IRSF sample (blue bars). We plot the

distributions of the difference in color in Figure 5. We found an average offset $\delta(J - K_S)$ between the mean colors from the CPAPIER sample and the reference data of -0.06 mag (solid magenta line), which is a factor of two larger than the offset from the IRSF sample (-0.03 mag , solid blue line). However, mean magnitudes of brighter Cepheids (i.e. $\log P \gtrsim 1.4$ or $J \lesssim 12.5 \text{ mag}$), from the CPAPIER sample have a better photometric precision than the IRSF data, as indicated by the distribution of the magenta dots in Figure 4. Thus, we decide to include CPAPIER mean magnitudes for brighter Cepheids. Finally, in the right panel of the same Figure, we perform a similar comparison also for 76 FO Cepheids in the VMC sample, and we find very similar results: -0.09 mag for CPAPIER and -0.03 mag for IRSF. As already anticipated (see, e.g., I15), we found that a single-epoch precise photometric measurement, together with the use of light curve templates, allows us to estimate individual Cepheid distances with an accuracy better than mean Cepheid magnitudes based on poor photometric quality and randomly sampled light curves.

We end up with a sample of $\sim 4,000$ Cepheids (2308 FU and 1699 FO) for which we obtained I, V, J, H , and K_S mean magnitudes (Sample A). Their distribution onto the plane of the sky is shown in Figure 1. For $\sim 65 \%$ of them we also have $w1$ -band mean magnitudes. This other sample (Sample B) includes $\sim 2,600$ Cepheids (1557 FU and 1086 FO), for which we have optical-NIR and MIR mean magnitudes. A schematic summary of the samples adopted is given in Table 1.

The new sample described here is the first optical-NIR-MIR dataset for Cepheids entirely covering the LMC disk, thus, allowing us to investigate its physical properties. In particular, we adopt the Sample A, which is

larger, to determine the LMC disk geometry, while we adopt the Sample B, which includes the MIR data, to determine the reddening and the mean distance to the LMC disk. The key advantage in our approach is that we are using a homogenous young stellar tracer for which we can also carefully quantify systematic errors.

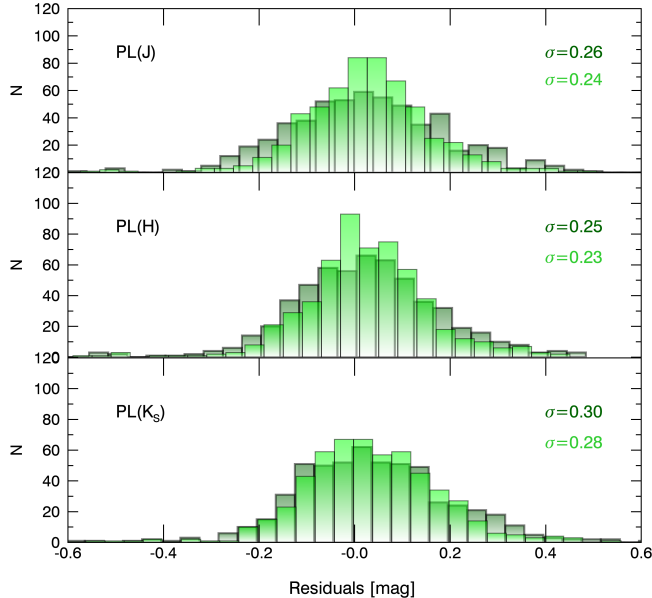


FIG. 4.— Quantitative representation of the improvement on the determination of NIR mean magnitudes by applying NIR templates to the 2MASS single-epoch observations.

Top: Comparison between the residual distribution around the PL relation in the J -band for single-epoch (dark green) and template corrected (light green) magnitudes. In the assumption of Gaussian distribution, the standard deviations σ of the two samples are also labeled in the top right corner. By applying the NIR templates, the scatter is reduced of the $\sim 8\%$ with respect to the use of 2MASS single-epoch magnitudes. Middle: The same as top but for the H -band. Bottom: The same as top but for the K_S -band.

3. OPTICAL AND NIR PERIOD–WESENHEIT RELATIONS

Using the five available mean magnitudes of our Sample A, and adopting the reddening law by Cardelli et al. (1989) with $R_V = \frac{A(V)}{A(B)-A(V)} = 3.23$ (Fouqué et al. 2007), we can define different Wesenheit indices. Once the reddening law has been fixed, these photometric indices are reddening-free pseudo-magnitudes that can be constructed using either two or three apparent magnitudes. The first column in Table 2 summarises the adopted Wesenheit indices. Optical-NIR Wesenheit relations are minimally affected by uncertainties on the adopted reddening law, and they are also marginally affected by metallicity effects (Inno et al. 2013). Moreover, they are also linear over the entire period range and, because they mimic a period-luminosity-color relations, they have a smaller intrinsic dispersion (σ_{ID}) caused by the width in temperature (color) of the Cepheid Instability Strip (IS).

Although, the intrinsic dispersion is expected to be small, it is not negligible. We can use up-to-date theoretical models for classical Cepheids to quantify it. The predicted IS has been computed using the non linear approach to stellar pulsation detailed in Bono et al. (1999b)

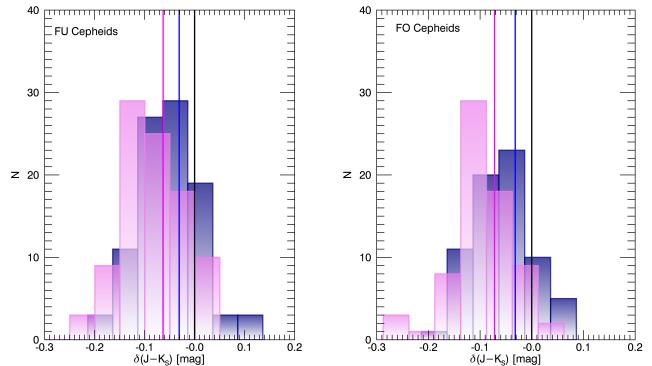


FIG. 5.— Left: Distributions of the offsets between the mean colors of the selected reference FU Cepheids from the P04 and VMC samples and the ones from the CPAPIER sample (magenta bars) and from the IRSF sample (blue bars). Right: Distribution of the offsets between the mean color of reference FO Cepheids from the VMC sample, and the ones from the CPAPIER sample (magenta bars) and from the IRSF sample (blue bars). In both panels, the black solid lines indicate the reference mean color, while the blue lines indicate the mean offset for the IRSF sample: -0.03 mag (FU,FO) and the magenta lines indicate the mean offset for the CPAPIER sample: -0.06 mag (FU), -0.09 mag (FO).

The evidence that the mean offset of the mean colors from the CPAPIER sample is a factor of 2–3 larger with respect to the ones in the IRSF sample demonstrates that the use of NIR templates together with accurate single-epoch observations provides J and K mean magnitudes that are more accurate than the ones obtained from light curves with poor photometric accuracy.

that includes a time-dependent treatment of the convection. We then built a synthetic population to fill this IS for the average metallicity of the LMC, i.e. $Z=0.008$. This is done by assuming a mass distribution that follows the relation M^{-3} and spans from 3 to $12 M_{\odot}$. We then associated a period to each synthetic star using both a pulsation and a mass–luminosity relation given from evolutionary theory (see also Bono et al. 1999,b, 2000; Marconi et al. 2005; Fiorentino et al. 2013). Finally, using the updated bolometric corrections provided by F. Castelli¹³, we derive the Wesenheit relations in all the desired magnitude and color combinations.

All the theoretical optical-NIR PW relations obtained for $\sim 1,300$ synthetic stars are listed in Table 2, together with their scatter. The smaller is the intrinsic dispersion (from up to down), the more accurate the determination of Cepheid individual distances will be. An inspection of Table 2 shows that NIR PW relations have smaller intrinsic dispersions when compared to optical and optical-NIR ones. In particular, the PW_{JH} and PW_{HJK} relations show the smallest dispersions, which are two–three times smaller than the one found around the PW_{VI} relation. Thus, Cepheid individual distances estimated on the basis of these relations appear to be less affected by systematic errors due to the intrinsic width of the instability strip. However, the photometric errors on observed NIR mean magnitudes are still significantly larger than the optical ones.

The photometric uncertainty on the OGLE-IV mean magnitudes, computed by adopting the standard deviation of the 7th-order Fourier-series fit to the V - and I -band light curves, is 0.007 mag for brighter Cepheids ($0.7 \leq \log P \leq 1.5$) and 0.02 mag for fainter

¹³ see <http://www.oact.inaf.it/castelli/castelli/odfnew.html>

ones ($\log P < 0.7$). The photometric error in the J -band ranges from 0.005 mag (VMC, P04) to 0.03 mag (2MASS) for brighter Cepheids ($0.7 \leq \log P \leq 1.5$) and from 0.05 to 0.15 mag (2MASS) for fainter ones ($\log P < 0.7$). Such larger uncertainties somehow limit the use of NIR photometry to determine individual Cepheid distances. Figure 6 shows the effect of the uncertainty on the NIR PW_{HJK} relations. The A) panel of this Figure shows the W_{VI} magnitudes as a function of the logarithmic period for our theoretical models (cyan dots) and by adopting an LMC distance modulus equal to 18.45 mag (Inno et al. 2013). The standard deviation σ around the best-fit relation is labeled in the top of the panel. This standard deviation refers *only* to the σ_{ID} . A similar plot but for the W_{HJK} is shown in the B) panel of the same Figure. In this case, the standard deviation is a half of the one around the optical PW relation. We now simulate the photometric errors on the mean magnitudes of the theoretical models. We adopted the photometric errors shown in Figure 3 for the IRSF sample. We model the photometric error with a second-order polynomial function and then compute the error associated to each predicted magnitude from the polynomial fit and by performing a random extraction from a Gaussian with the same standard deviation as the observed one ($\sigma \sim 0.3$ mag). The new relation is shown in the C) panel of Figure 6. The scatter around the relation is now due to the σ_{ID} and the photometric error on the mean magnitudes. We find that the dispersion is now similar to the σ_{ID} of the optical PW relations.

Finally, we also assume the photometric errors associated to the 2MASS sample ($\sigma \sim 0.7$ mag). The new PW_{HJK} relation is shown in the D) panel of the same Figure. The standard deviation around the theoretical best-fit relations is now of the order of 0.2 mag, which is a factor three larger than the σ_{ID} of the optical PW relations. Thus, the potential of NIR PW relations for accurate Cepheid individual distance determinations is still limited by the current photometric precision.

3.1. Observed PW relations

We derive PW relations in the form $W = a + b \log P$ for all the Cepheids in our Sample A. We performed an iterative sigma-clipping (biweight procedure, Fabrizio et al. 2011) and a six-sigma outlier cut to perform the outlier rejection before the fitting. The results for all the PW relations are listed in Table 3, while W_{VI} (left) and NIR W_{HJK} (right) PW relations are also shown in Figure 7.

Note that the current value of the slope for the PW_{VI} relation differs at the $2.3\sigma_b$ level with the slope found by Jacyszyn-Dobrzniecka et al. (2016, $b = -3.327 \pm 0.001$ vs $b = -3.313 \pm 0.006$). However, the difference is vanishing if we consider the dispersion around the relation, namely $\sigma = 0.08$ mag for both the above estimates. The marginal difference in the slope is the consequence of different assumptions in dealing with outliers, namely 3σ (Jacyszyn-Dobrzniecka et al. 2016) vs 6σ (ours). Using the same σ clipping we find $a = 15.888 \pm 0.004$ and $b = -3.320 \pm 0.006$, which perfectly agree with the values found by Jacyszyn-Dobrzniecka et al. (2016). However, the latter cut removes 15% of the Cepheids in the sample, while the former only the 3%. Note that the standard deviations of the PW_{VI} relation is minimally

affected by the different assumptions concerning the σ clipping ($\sigma = 0.08$ mag in the case of the 6σ -clipping, and $\sigma = 0.06$ mag in the case of the 3σ -clipping). The last column in Table 3 gives the standard deviation around the best-fit for all the PL and PW relations derived in this investigation.

The observed standard deviation for the PW_{VI} relations is, as expected, smaller than the ones of the PW_{JH} and PW_{HJK} relations, given the higher accuracy of the OGLE photometry. In fact, the standard deviation decreases for all the Wesenheit indices that include optical data, because they are affected by smaller photometric errors when compared with purely NIR Wesenheit.

By adopting all these different relations, we can obtain different distance estimates for each star, with associated errors that are given by the propagation of the uncertainty on the mean magnitude and the uncertainty on the slopes of the PW relation adopted, plus the systematic error given by its intrinsic dispersion, as described in the following.

3.2. Errors on the Cepheid individual distance moduli

The measurement error on the individual distance moduli obtained by adopting the PW_{VI} relation is the sum in quadrature of the photometric error on the Wesenheit mean magnitudes and the error on the slope σ_b , which is anyway negligible (0.001 mag). This means that the error can be propagated directly from the photometric error on the optical mean magnitudes, and ranges from 0.01 mag (brighter Cepheids) to 0.04 mag (fainter Cepheids), i.e. 1%–3% in distance. On the other hand, theoretical predictions give us an upper limit for the systematic error related to the ID, which is 0.06 mag, or $\sim 5\%$ in distance. Summarising, while the precision of Cepheid individual distances based on the PW_{VI} is better than 3%, the accuracy is limited to $\sim 5\%$. If we use the PW_{HJK} relations, the errors on individual distance moduli ranges from 0.03 mag ($\log P > 0.7$) to 0.10 mag ($\log P < 0.7$), if we exclude the 2MASS sub-sample, and to 0.15 mag if we include it, which translates to 2%–15% in distance. Instead, if we choose the PW_{JH} relations, errors are even larger (up to 20%) as a consequence of the larger coefficient adopted in the Wesenheit definition ($\frac{A_H}{E(J-H)} = 1.630$) respect to the one in the W_{HJK} ($\frac{A_K}{E(J-H)} = 1.046$). Moreover, Inno et al. (2013) found that the PW_{JH} relation are more affected by uncertainties on the slope of the reddening law. Thus, we adopted the NIR PW_{HJK} relation, which is minimally affected by such uncertainty. In fact, the uncertainty on the assumed reddening law also contributes to the systematics.

Recently, De Marchi et al. (2016) found that in the 30 Doradus star forming region, the reddening law changes and in particular the total-to-selective extinction is $R_V = 4.5$, thus larger than the one adopted here, i.e. $R_V = 3.23$. However, if we compute the coefficient of the W_{HJK} corresponding to $R_V = 4.5$, we find a discrepancy lower than 1% (1.041 vs 1.046), which minimally affects our results, while for the optical bands this discrepancy is of the order of 20% (1.70 vs 1.55). If we assume $R_V = 4$, we find a slope of the PW_{VI} relation which is steeper of 0.04 mag with respect to the one listed in Table 3, while the slope of the PW_{HJK} relation only changes of 0.01 mag. Thus, the systematic error due to the uncertainty

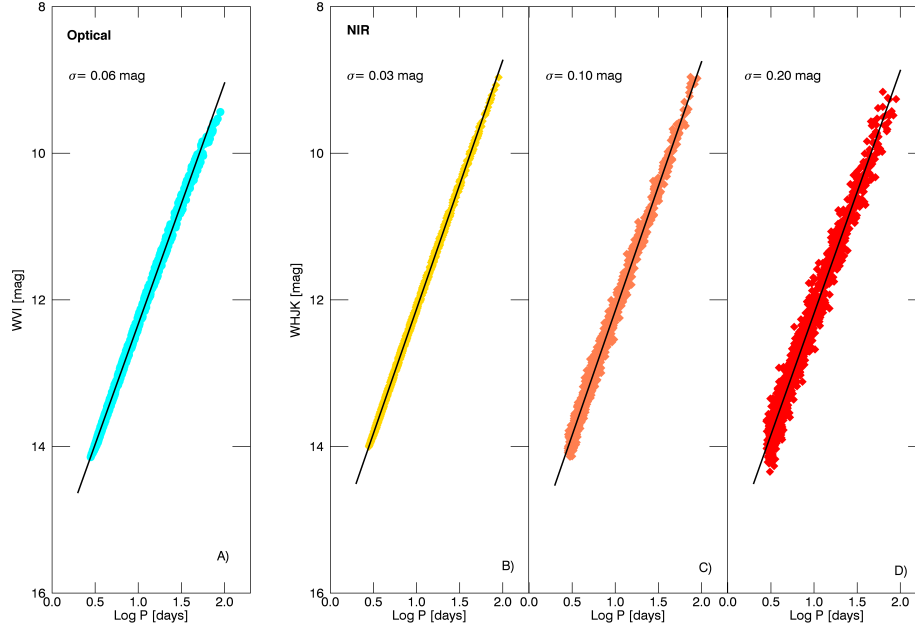


FIG. 6.— Panel A): PW_{VI} relation for theoretical models. The line shows the the best-fit relation, while the standard deviation around the fit is labeled in the top left corner of the Figure. Panel B): PW_{HJK} relation for the same theoretical models. The intrinsic dispersion due to the finite width of the Instability Strip is a factor 10 smaller respect to the one found for the optical relation ($\sigma=0.01$ mag vs $\sigma=0.10$ mag). Panel C): The same relation for theoretical model but now we include photometric errors, simulated on the basis of our IRSF sub-sample. The dispersion around the best-fit increases to 0.12 mag because of the photometric error. This means that the dispersion is now similar to the PW_{VI} one. Panel D): The same as in Panel C) but the photometric error has been simulated on the basis of our 2MASS sub-sample. The dispersion around the best-fit increases to ~ 0.20 mag because of the larger photometric errors. The comparison between the dispersions σ in the NIR and in the optical bands shows that the potential of NIR PW relations for determining accurate Cepheid individual distances is limited by the photometric precision of the NIR mean magnitudes available.

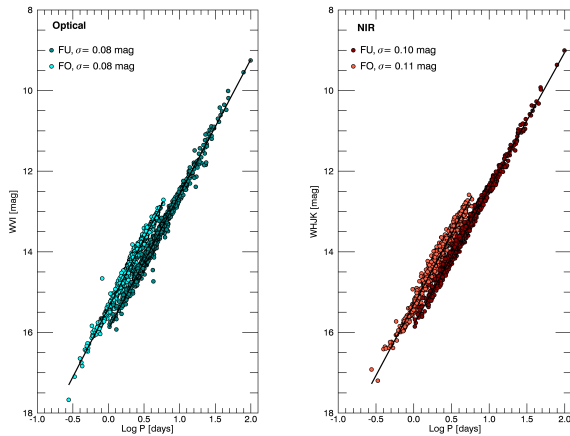


FIG. 7.— Observed optical W_{VI} (left) and NIR W_{HJK} (right) PW relations (solid lines) for FU and FO Cepheids. The dispersions around the best-fits are also labeled in the top. The residuals of the best-fit relations have been adopted to derive Cepheids' individual distances and, in turn, their three-dimensional distribution. The best-fit parameters of each relation are given in Table 3.

on the total-to-selective absorption ratio is at 2% level for the optical and at 0.5% level for the NIR. Moreover, the theoretical predictions in Table 3 indicate that the ID for the PW_{HJK} relation is $\lesssim 0.03$ mag, which corresponds to an accuracy better than 2% on the individual distance estimates. Thus, the precision of Cepheid individual distances based on the PW_{HJK} highly depend on the sub-sample adopted, and it ranges from 2% to 10%, when excluding the 2MASS sub-sample, and to 15% when including it, while the systematic effects are lower

than 2%. Concluding, Cepheids distances derived on the basis of optical relations are affected by significant systematics ($\sim 7\%$), while distances derived on the basis of NIR relations are mostly limited by measurement errors (2%–15%).

4. DISTANCE MEASUREMENTS

We adopted the PW_{VI} and PW_{HJK} relations listed in Table 3 for the FU and FO Cepheids in order to estimate the distances to all the Cepheids in our Sample A.

The individual relative distance moduli have been estimated by calculating the differences:

$$\begin{aligned} \delta\mu_{0,i,VI} &= W_{i,VI} - (a_{VI} + b_{VI} \log P_i), \quad (1) \\ \delta\mu_{0,i,HJK} &= W_{i,HJK} - (a_{HJK} + b_{HJK} \log P_i), \quad (2) \end{aligned}$$

where a and b are the coefficients in Table 3 for the corresponding PW relations and W_i is the mean Wesenheit magnitude for the i -th star in the given bands. Figure 8 shows the projection onto the plane of the sky of the Cepheids in our sample, color coded by their individual relative distance moduli obtained by adopting the optical PW_{VI} relation (left panel) and the NIR PW_{HJK} relation (right panel). The color coding clearly shows that that the eastern parts of the LMC bar and northern arm are closer to us (negative distance moduli) with respect to the western regions (positive distance moduli), thus indicating that the LMC is not seen face-on, but it is inclined respect to the plane of the sky (see also Weinberg & Nikolaev 2001; van der Marel & Cioni 2001; van der Marel & Kallivayalil 2014; Jacyszyn-Dobrzyniecka et al. 2016). In order to measure such viewing angles, we

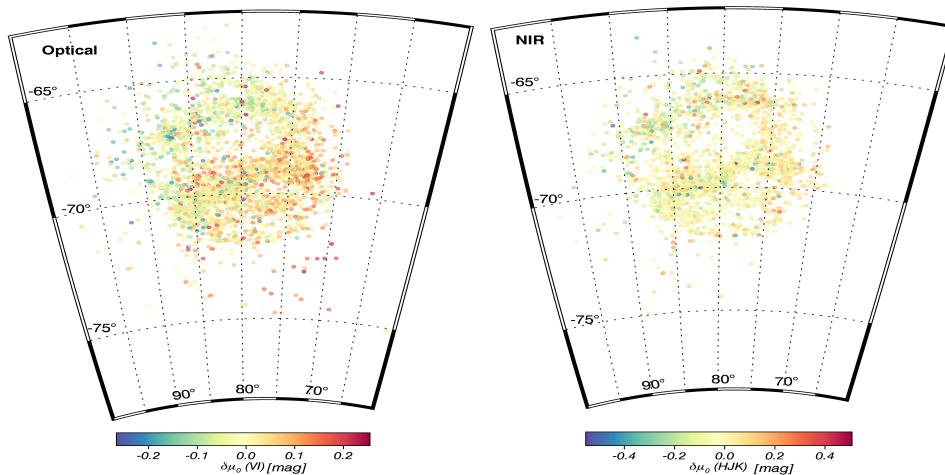


FIG. 8.— Sky distribution of the Cepheids in the Sample A (FU+FO) color coded by their relative distance moduli (mag) obtained by adopting Equations 1 for the optical PW_{VI} relation (left) and the NIR PW_{HJK} relation (right). Both the distributions show similar features, with the eastern part of the LMC closer to us (negative relative distance moduli) respect to the western region (positive relative distance moduli). The relative distance moduli shown here have been transformed into absolute distances according to Equation 4 and used to derive the viewing angles of the LMC plane.

first need to convert the relative distance moduli given by Equation 1 into individual absolute distances (kpc). We adopted the standard formula

$$D_i = 10^{[0.2 \times (\delta\mu_{0,i} + \mu_{0,LMC}) - 2]}, \quad (3)$$

where $\mu_{0,LMC} = 18.483$ mag is the mean distance modulus to the LMC (Pietrzyński et al. 2013, hereinafter P13), corresponding to the distance $D_0 = 49.97$ kpc. Thus, we use the individual distances D_i to move into the cartesian reference system introduced by Weinberg & Nikolaev (2001) and Nikolaev et al. (2004). This new reference system (x, y, z) has its origin at the centre of the galaxy, defined by the position $(\alpha, \delta, D) \equiv (\alpha_0, \delta_0, D_0)$. The z -axis is pointed towards the observer, the x -axis is anti-parallel to the α -axis and the y -axis is parallel to the δ -axis. The (x_i, y_i, z_i) coordinates for each Cepheid are then obtained using the transformation equations

$$\begin{aligned} x_i &= -D_i \sin(\alpha_i - \alpha_0) \cos \delta_i, \\ y_i &= D_i \sin \delta_i \cos \delta_0 - D \sin \delta_0 \cos(\alpha - \alpha_0) \cos \delta_i, \\ z_i &= D_0 - D_i \sin \delta_i \sin \delta_0 - D \cos \delta_0 \cos \delta_i \cos(\alpha_i - \alpha_0). \end{aligned} \quad (4)$$

Because of its non-axis-symmetric shape, the LMC disk does not have a very well defined center. Thus, the definition of $(\alpha_0, \delta_0, D_0)$ is somewhat arbitrary and van der Marel & Cioni (2001) showed that it does not affect the results. We estimated the center of the Cepheid distribution by computing the Center of Mass as follows:

$$CM_u = \frac{\sum_i w_i u_i}{\sum_i w_i},$$

where u_i are the coordinates α and δ of the i -th star and the weights w_i is given by its inverse distance in the 2D-space (α, δ) . To compare our results with similar findings from other authors, we also adopted four different locations for the center of the distribution available in the literature. Table 4 lists all the adopted values together with their ID. In particular, we adopted the center of the rotation map of the HI estimated by Kim et al. (1998, CII_{LMC}), the center of the visual-band isophotes estimated by de Vaucouleurs & Freeman (1972, CIII_{LMC})

and the geometrical center estimated by Nikolaev et al. (2004, CIV_{LMC}) from 2MASS data for LMC Cepheids.

5. LMC VIEWING ANGLES

Once we have the x_i, y_i , and z_i for each star in the cartesian system, we derive the orientation, i.e., inclination i and position angle P.A., of the LMC disk, by fitting a plane solution of the form:

$$z = Ax + By + C; \quad (5)$$

To estimate the best-fitting plane, we performed a least-squares method where x and y has been considered the independent variables. In fact, from Equation 4 follows that the error on z_i is larger the errors on x_i and y_i . The dominant term in the error budget is given by the uncertainty on the distance D_i , since the positions on the sky (α, δ) are known with a precision better than $0''.2$ (Jacyszyn-Dobrzniecka et al. 2016) from the OGLE catalog. In particular,

$$\sigma_{x,y} \propto \frac{\sigma_D}{D}(x, y);$$

while the error on z_i also accounts for the uncertainty on D_0 :

$$\sigma_z \propto \sqrt{\frac{\sigma_D^2}{D} z^2 + \frac{\sigma_{D_0}^2}{D_0}}.$$

Figure 9 shows a comparison between the errors σ_z for distances obtained from the optical PW relations (left) and for the ones based on the NIR PW relations (right). The Cepheids are plotted in the x, y plane and color-coded by their error σ_z on z , which ranges from ~ 0.5 kpc (optical, NIR) to $\lesssim 1$ kpc in the case of the optical data, and to $\lesssim 4.5$ kpc in the case of the NIR data. However, we find an error $\sigma_z > 1$ kpc only for the Cepheids belonging to the 2MASS sub-sample. Thus, the limited photometric accuracy on the 2MASS data is the main culprit of the limited accuracy of our results based on the NIR distances.

Finally, note that parameter C in Equation 5 is introduced to remove any possible bias due to arbitrariness

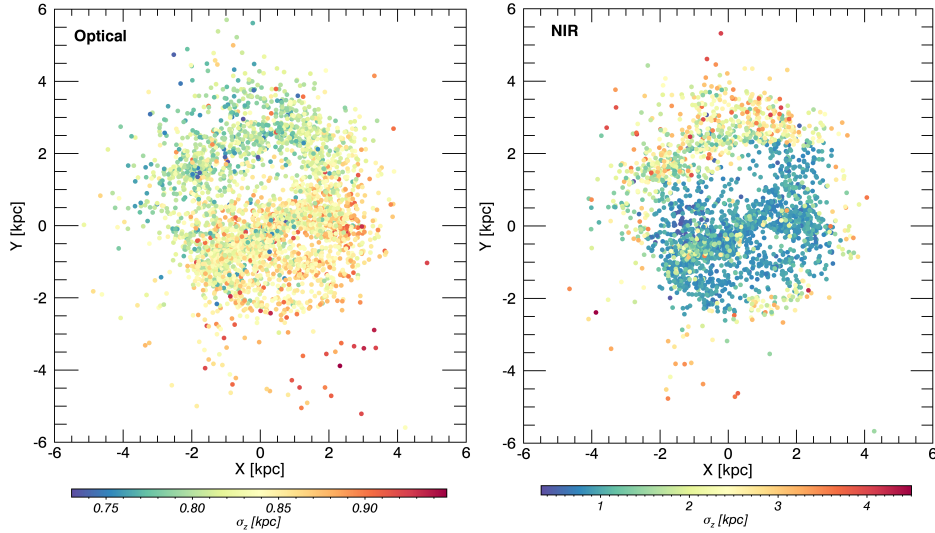


FIG. 9.— Comparison between the measurement errors on z in the case of distances derived from the optical PW_{VI} relation (left) and from the NIR PW_{HJK} relation (right). The error on z is obtained by propagating the uncertainty on D_0 and the ones on the individual distance moduli D_i , which are essentially given by the error associated to the mean magnitudes in the different bands. The errors on z are similar for optical and NIR individual distances *only* in the case of our most accurate sub-samples, i.e. P04, VMC, IRSF and CPAPIER, while they are up to four times larger for the 2MASS sample. The low photometric accuracy of the 2MASS sub-sample is the main culprit of the limited accuracy of our results based on NIR data.

in the definition of the central position. The constant C would be zero if the origin of our coordinate system $(\alpha_0, \delta_0, D_0)$ corresponds to the center of the LMC disk plane. We found $C \lesssim 10^{-3}$ kpc for our CI, and less than 1 kpc in the case of the adopted center: CII, CIII CIV, and CV. This indicates a negligible discrepancy between these positions and the center of the population traced by the Cepheids. We can also estimate the error associated to our best-plane solution, by calculating the standard deviation, and we found $\sigma_{zfit} = 1.7$ kpc. Figure 10 shows the three-dimensional distribution of the Cepheids in the x, y, z space in the case of distances determined by adopting the optical (left) and NIR (right) PW relations. The best-fitting planes are also shown as shaded surfaces.

From the coefficients A, B and C in Equation 5 we derive the position angle P.A. and the inclination i of the disk

$$P.A. = \arctan\left(-\frac{A}{B}\right) + \text{sign}(B)\frac{\pi}{2},$$

$$i = \arccos\left(\frac{1}{\sqrt{A^2 + B^2 + 1}}\right). \quad (6)$$

The ensuing errors on the above angles can also be determined by propagating the errors on the best-fit parameters as discussed in the following section. The values we found for the LMC are listed in Table 5, together with a list of literature values for comparison.

5.1. Error budget on the viewing angles

By assuming that C is a constant while the coefficients A and B are independent, we can use the standard error propagation formula, i.e.,

$$s_f = \sqrt{\left(\frac{\partial f}{\partial A}\right)^2 s_A^2 + \left(\frac{\partial f}{\partial B}\right)^2 s_B^2} \quad (7)$$

where f is one of the functions defined by Eq. 6. Once we compute the derivative, we find:

$$s_{P.A.} = \frac{1}{A^2 + B^2} \sqrt{B^2 s_A^2 + A^2 s_B^2}, \quad (8)$$

and

$$s_i = \frac{1}{A^2 + B^2 + 1} \frac{1}{\sqrt{A^2 + B^2}} \sqrt{A^2 s_A^2 + B^2 s_B^2} \quad (9)$$

The coefficients A and B are equal to $A = -0.394 \pm 0.009$ and $B = 0.223 \pm 0.009$ when adopting the optical PW relation, and to $A = -0.419 \pm 0.011$ and $B = 0.234 \pm 0.011$ when using the NIR PW relation. By propagating the errors according to Equations 8 and 9, we found $s_{P.A.} = 0^\circ.02$ and $s_i = 0^\circ.01$ in the case of viewing angles determined on the basis of the optical data, and $s_{P.A.} = 0^\circ.02$ and $s_i = 0^\circ.02$ in the case of the NIR data. The errors associated on the coefficients are computed according to the least-square method we adopted for the fit. We used the IDL package MPFIT¹⁴ to perform the fit, which provides the formal 1- σ error for each parameter, computed from the covariance matrix, where individual measurements are weighted with the inverse of the associated error. The errors on x_i, y_i and z_i for each star have been computed as described in the previous section.

6. COMPARISON WITH PREVIOUS ESTIMATES

Data listed in Table 5 display several interesting features worth being discussed in more detail.

i) Internal consistency—The current estimates of the P.A. (column 2) and of the inclination (column 3) are, within the errors, minimally affected by the adopted center. Moreover and even more importantly, we provided independent estimates using optical and NIR mean magnitudes. The two data sets are affected by different measurements and systematic errors, as already discussed

¹⁴ <http://cow.physics.wisc.edu/~craig/idl/idl.html>

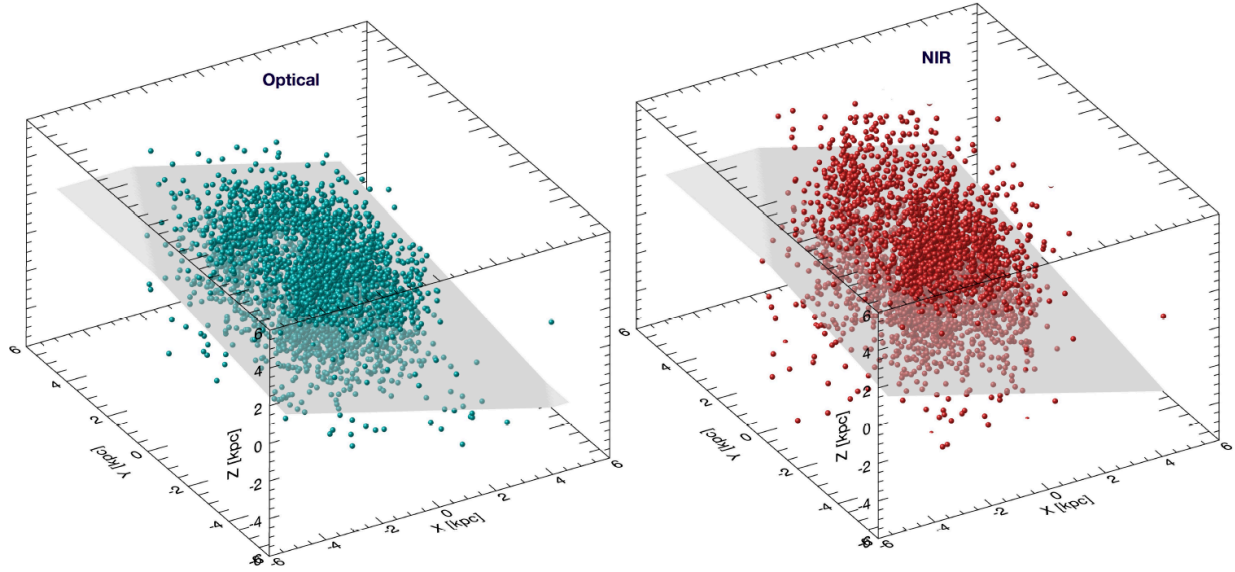


FIG. 10.— Three-dimensional distribution of the LMC Cepheids in our Sample A. Distances have been determined by adopting the optical PW_{VI} relation (left) and the NIR PW_{HJK} relation (right). The grey shadowed area shows the best-fit plane from which we can derive the LMC viewing angles. A qualitative comparison between the two panels shows that the three-dimensional distribution of the LMC Cepheids as mapped by the optical data is very similar to the one mapped by the NIR ones. However, the larger scatter in z observed in the northern spiral arm for the right panel with respect to the left panel is a consequence of the larger photometric error of the NIR data from the 2MASS sub-sample respect to the optical data.

in Section 3. Therefore, we can perform an average to obtain our best estimate and adopt the spread in the values as a solid estimate of the systematic error: $i = 25^\circ.05 \pm 0^\circ.02$ (statistical) $\pm 0^\circ.55$ (systematic) and $P.A. = 150^\circ.76 \pm 0^\circ.20$ (statistical) $\pm 0^\circ.07$ (systematic). We also compared the LMC viewing angles obtained by adopting independently either FU or FO Cepheids and we found that the P.A. differ of $\sim 0^\circ.16$ (optical) and $\sim 0^\circ.48$ (NIR), while inclinations differ of $\sim 0^\circ.4$ (optical) and $\sim 3^\circ.5$ (NIR). However, the values based on FU Cepheids agree within 1σ with the values based on the entire sample, and with the adopted best value. The viewing angles based on FO Cepheids differ of about at 4σ level ($\lesssim 0^\circ.1$) with the solution based on the entire sample and with the adopted best value. The above difference between FU and FO Cepheids appears the consequence that FO Cepheids account for less than 40% of the entire sample. The spatial distribution of FU and FO Cepheids shows also some diversity, with the FO Cepheids more extended in the outer disk when compared with the FU ones (see, e.g., Figure 1). To quantify the quoted variations we also investigated the change in viewing angles as a function of the distance from the center of the LMC. The results are shown in Figure 11, where the variation in inclination and P.A. are plotted as a function of the radius, in the case of distances based on the optical (dark cyan dots) and on the NIR (dark red dots) data. In the left panel of this Figure, the distribution in the plane x,y of the LMC Cepheids is shown. We defined circular regions in this plane, with radius from 0.5 to 6.5 kpc with a step of 0.5 kpc, and considered all the Cepheids included inside such regions to determine the viewing angles. The values found at different radii are plotted in the left panel and show that values based on Cepheids located inside a radius of ~ 3 kpc from the center differ significantly from the values based on larger

area. This is not surprising, since the central regions are dominated by the bar and have a complex geometry. Moreover, the discrepancy between viewing angles based on optical and NIR data in these regions might be related to a possible change of the reddening law in the more extinguished regions of the LMC bar (De Marchi et al. 2016). On the other hand, values based on the outer regions are in excellent agreement with each other, and there is no solid evidence of a change of the viewing angles with radial distance.

ii) External consistency—The current estimates of LMC viewing angles agree well with similar estimates based on classical Cepheids available in the literature. The excellent agreement between our values and the values found by Jacyszyn-Dobrzyniecka et al. (2016), on the basis of the same sample from the OGLE-IV CCs demonstrates once again the robustness and precision of the approach adopted. The position angle derived by Nikolaev et al. (2004) from independent datasets agrees also very well with our best estimate, while their inclination is larger. The difference in inclination is likely due to the improved accuracy on mean NIR magnitude from single epoch measurements (see Section 2 and their Section 3.2) and also to the sample (our sample is a factor 2 larger, see also Section 8).

The comparison with the estimates provided by P04 indicates a good agreement for the inclination, but a 2σ difference in the PA. However, their sample is again significantly smaller (92 vs $\sim 3,700$) and biased towards brightest stars. Similar arguments apply to the estimate provided by Haschke et al. (2012), since they only adopted optical mean magnitudes provided by OGLE-III, which was limited to a smaller area close to the LMC bar.

iii) Age consistency—Recent estimates of the LMC viewing angles provided by van der Marel & Kallivay-

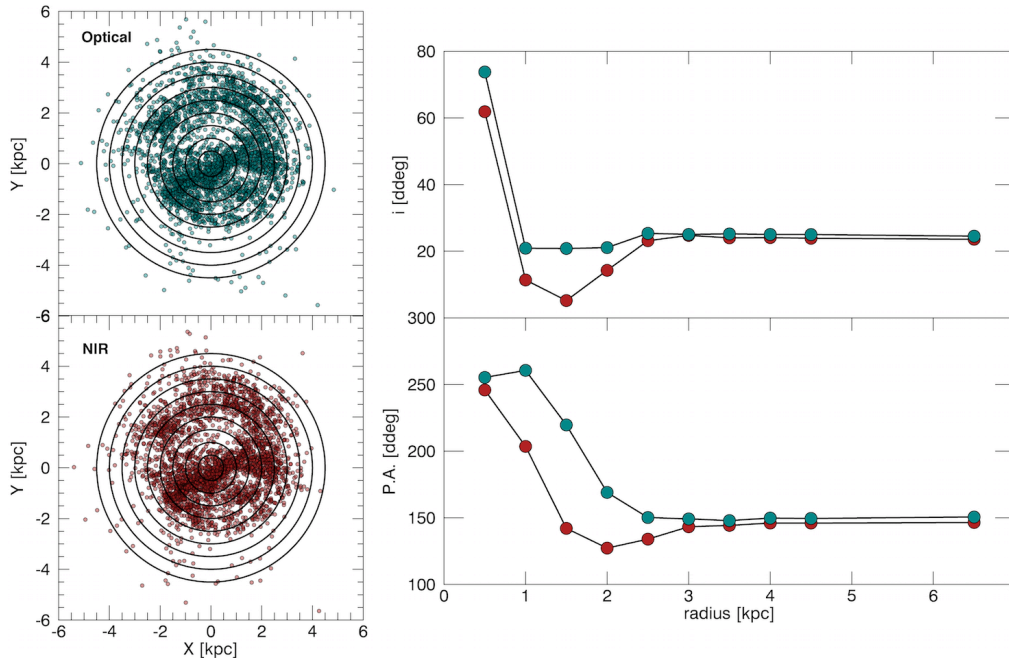


FIG. 11.— Variation of the viewing angles of the LMC disk as a function of the radial distance (in kpc). Left: The LMC disk is divided into concentric annuli with different radii, starting from 0.5 to 6.5 kpc with a steady increase of 0.5 kpc. The annuli are over-plotted on the Cepheids’ spatial distribution in the x,y plane based on the optical (top) and NIR (bottom) PW relations. Right: The upper panel shows the variation of inclination as a function of the radial distance, while the lower panel shows the variation of the P.A., for distances based either on optical (dark cyan) or on NIR (dark red) PW relations.

alil (2014) using Red Super Giants (RSGs) agree quite well with current estimates. This is an interesting findings for a twofold reason: *a)* The quoted authors adopted a completely different approach to estimate the viewing angle, based on kinematics. *b)* The difference in age from short- to long-period LMC Cepheids, estimated on the basis of period-age relations, is of the order of 300 Myr, while RSG have typically ages of few tens of Myr (Bono et al. 2015). Thus, the similarity between the geometrical proprieties of the two tracers implies that RSGs and Cepheids belong to the same young population.

iv) Comparison with intermediate-age stellar populations—The LMC viewing angles provided by Subramanian & Subramaniam (2013) using RC stars agree quite well with current estimates. This is an interesting finding, given that the accuracy of individual distances of RC stars is still lively debated in the literature, since it might be affected by differences in the underlying stellar populations. The LMC viewing angles estimated by van der Marel (2001) using AGB stars show a difference at the 2σ level. It is not clear whether the difference is mainly caused by the LMC area covered by their sample, which extends further than the region were Cepheids are located, or by a possible mix of old and intermediate-age AGB stars.

v) Comparison with old stellar populations—Very accurate LMC viewing angles have been recently provided by Deb & Singh (2014) using a large sample ($\sim 13,000$) of RR Lyrae stars covering a significant fraction of the LMC body. They found a position angle that is at least 25 degrees larger than the current one, moreover, the inclination angle is at least two degree smaller. This difference taken at face value is further confirming that old and young stellar populations in the LMC have different

radial distributions and likely a different center of mass.

Similar differences in radial distributions have already been found in several nearby dwarf galaxies (Monelli et al. 2003; Bono et al. 2010). This difference also appears in the chemical composition of the two populations. Indeed, Fabrizio et al. (2015) found evidence that the old and intermediate-age populations in the Carina dwarf spheroidal display different mean iron and magnesium abundances. Thus suggesting that they experienced different chemical enrichment histories. A similar empirical scenario is also disclosed by LMC Cepheids and RR Lyrae stars. Recent spectroscopic investigations based on high-resolution spectra indicate that the metallicity distribution of LMC Cepheids is centred on $[\text{Fe}/\text{H}] = -0.33$ with a standard deviation of 0.13 dex (Romaniello et al. 2008). On the other hand, spectroscopic measurements of LMC RR Lyrae based on low-resolution spectra (Clementini et al. 2000) indicate a mean $[\text{Fe}/\text{H}] \sim -1.5$ standard deviation of 0.5 dex.

The above evidence are further supporting the hypothesis that the LMC old and young stellar populations have had significantly different chemical enrichment histories.

In this context it is worth mentioning that the LMC viewing angles provided by van der Marel & Kallivayalil (2014) using RGs are quite different when compared with RR Lyrae stars. The inclination is more than 1.5σ larger, while the position angle is significantly smaller. A detailed analysis of the difference is beyond the aim of the current investigation. However, we note that RG are not “pure” old tracers, since intermediate-mass stars also contribute to the field population.

The use of a multi-wavelength fitting of the reddening law to apparent distance moduli of extra-galactic Cepheids, to determine their distances and reddening, was introduced by Freedman et al. (1985, 1991) and has been recently revised by Rich et al. (2014).

The above method is based on the evidence that the true distance modulus of the i -th Cepheid belonging to a stellar system can be written in the following form:

$$\mu_{0,i} = \mu_{obs,i}(x) + (a(x)R_V + b(x)) \times E_i(B - V) \quad (10)$$

where $x \equiv \lambda^{-1}$, $a(x)$ and $b(x)$ are the coefficients of the adopted reddening law (Cardelli et al. 1989). Fitting this relation to the apparent distance moduli of the same Cepheid estimated using different photometric bands and by extrapolating to $x \sim 0$, we can determine its true distance modulus. Adopting the observed PL relations in the V, I, J, H, K_S and $w1$ -bands¹⁵ bands we can derive apparent distance moduli at six different wavelengths for all the Cepheids in our Sample B. The inclusion of the $w1$ -band mean magnitudes allow us to overcome possible systematics in the extrapolation to extremely long wavelengths. By assuming $R_V = 3.23$ and performing a fit of the above equation we can evaluate the true distance modulus and the color excess for individual Cepheids.

The zero-points of the six observed PL relations were calibrated following the same approach used in Inno et al. (2013). We adopted nine FU Cepheids for which HST parallaxes are available (Benedict et al. 2007; van Leeuwen et al. 2007). The FO PL relations were calibrated only using Polaris (van Leeuwen et al. 2007).

The optical and NIR mean magnitude of these calibrating Cepheids have been accurately measured (Benedict et al. 2007; Fouqué et al. 2007; Storm et al. 2011a), however, $w1$ -band light curves for the same Cepheids are not available, since they are saturated in the survey. Fortunately enough, the difference in the photometric zero-point between the $w1$ -band adopted by WISE and the $[3.6]$ -band adopted by SPITZER is vanishing (M. Marengo private communication). Therefore, the $w1$ -band FU and FO PL relations were calibrated using the mean $[3.6]$ magnitudes for calibrating Cepheids based on SPITZER observations provided by Marengo et al. (2010). Figure 12 shows the apparent distance moduli for three selected Cepheids in our sample (green, red and magenta dots) as a function of x and the best-fits estimated using Eq. 5 (green, red and magenta solid lines). The individual true distance moduli and the color excess are labeled together with their errors. The error bars also account for the systematic errors related to the position of the Cepheids inside the instability strip compared with the ridge line of the adopted PL relation. Individual distances based on PL relations rely on the assumption that the width in temperature of the instability strip can be neglected (Bono et al. 2002). On the other hand, distances based on PLC relations are not affected by this drawback (Bono et al. 1999b, 2002). To quantify this systematic error we adopted the standard deviations of theoretical PL relations in the above six bands and they are listed in Table 2. This is an upper limit to the standard deviations of the PL relations, since predictions cover the entire period range and uniformly fill the instability strip.

¹⁵ $x_V = 1.835\mu\text{m}^{-1}$; $x_I = 1.253\mu\text{m}^{-1}$; $x_J = 0.800\mu\text{m}^{-1}$; $x_H = 0.606\mu\text{m}^{-1}$; $x_K = 0.465\mu\text{m}^{-1}$; $x_{w1} = 0.286\mu\text{m}^{-1}$.

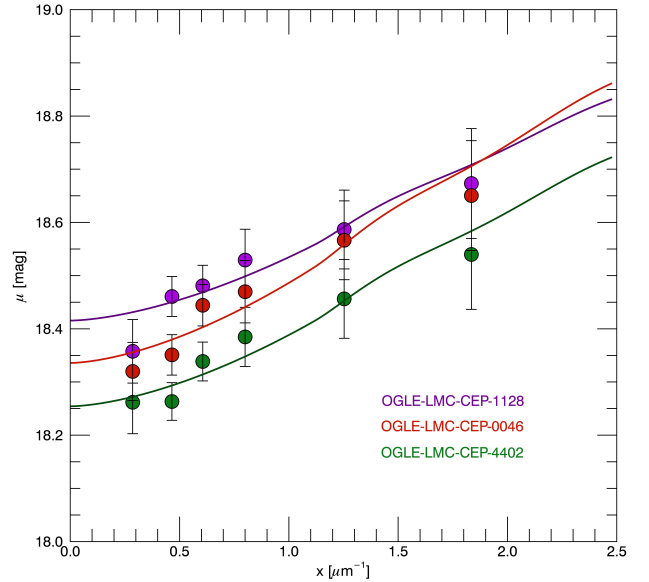


FIG. 12.— Apparent distance moduli (uncorrected for any reddening) for three different Cepheids (CEP-0107, purple; CEP-0683, green; CEP-2337, red) as a function of inverse wavelengths, with the associated error bars. The errors include both measurement and systematic effects. The best-fit of the reddening law is also showed (solid lines) for each of them (see Section 7 for more details).

Even a cursory look to the values listed in Table 2 shows that the standard deviations, as expected, steadily decrease for increasing wavelength. The difference is caused by the fact that cooler Cepheids become in NIR and in MIR systematically brighter due to a stronger sensitivity of the bolometric correction (Bono et al. 1999,b, 2000). In the case of the $w1$ -band we adopted the dispersion around the SPITZER $[3.6]\mu\text{m}$ PL relation provided by Ngeow et al. (2012), i.e., 0.025 mag.

The approach we adopted to estimate the error budget implies that we automatically weight more the apparent distance moduli based on NIR- and MIR mean magnitudes than the distances based on optical bands. The total error is then propagated on the parameters estimated by our least-squares fitting procedure. It is worth noting that current individual distance moduli, taking account for systematic errors, have an accuracy better than 1%, while individual extinctions have an accuracy better than 15%.

The individual reddening estimates were smoothed using a Gaussian kernel with a σ equal to the observed uncertainty. The smoothed reddening distribution was adopted to provide the reddening map shown in Figure 13. The star forming region of 30 Doradus stands out in the reddening map as the most extinguished region on the LMC bar, while on the other side of the bar, the star forming regions associated with NGC 1850 and NGC 1858 are also heavily extinguished and they can also be easily identified. The reddening across the LMC disk is, as expected, quite low with the exception of these peculiar regions.

7.1. Mean distance and reddening to the LMC

We also derived the average LMC true distance modulus and reddening. The statistical error associated to the

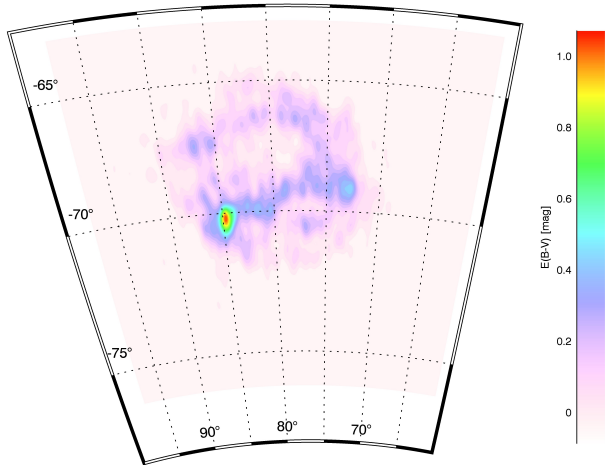


FIG. 13.— Reddening map of the LMC disk derived through the method described in Section 7. A Gaussian-smoothing has been applied to obtain the contour map. Individual values of the estimated reddening are given in Table 9.

distance modulus is dominated by the number of bands available, and in our case it is significantly small, and indeed the values range from 0.008 to 0.015 mag. Figure 14 shows the histogram of the distance moduli distribution for FU (blue bars) and FO Cepheids (red bars). We find a median distance modulus $\mu_0 = 18.48 \pm 0.10$ mag for both FU and FO pulsators, where the error is given by the standard dispersion around the median. The current distance moduli based on FU and FO Cepheids are in excellent agreement with each others and with the value recently published by P13, i.e., $18.493 \text{ mag} \pm 0.008$ (statistical) ± 0.047 (systematic). However, note that both distances and reddening values display neither a symmetric nor a Gaussian distribution. This means that the median values need to be cautiously treated. Thus, we only adopted the median value of the entire (FU+FO) sample for the purpose of comparing it to similar values in the literature and we found that our estimate $E(V - I) = 1.265 \times E(B - V) = 0.11 \pm 0.09$ mag, is in excellent agreement (within 1σ) with the value estimated by Haschke et al. (2011, hereinafter H11) using RC stars ($E(V - I) = 0.09 \pm 0.07$ mag), and RR Lyraes ($E(V - I) = 0.11 \pm 0.06$ mag).

However, individual distances and reddening are strongly related to the spatial distribution of the Cepheids in the LMC, as discussed in the previous Sections. Thus, we need to compare individual values and in particular we can compare $E(V - I)$ values for $\sim 1,000$ stars located at positions for which reddening from H11 is available. We download their catalog from the website: <http://dc.zah.uni-heidelberg.de/mcx>. The catalog provides mean reddening values for specific spatial bins whose coordinates are also available. We estimated the mean $E(V - I)$ values in the same spatial bins but from our reddening map. We first determined the number of Cepheids included in each bin, and we only considered bins that contain at least one Cepheid. We found ~ 500 bins that include from two to eight Cepheids. Finally, we estimated the difference in reddening from our mean values and the values by H11 for the same bin. We found that the difference is smaller than $1\sigma_{EVI}$ for $\sim 85\%$ of

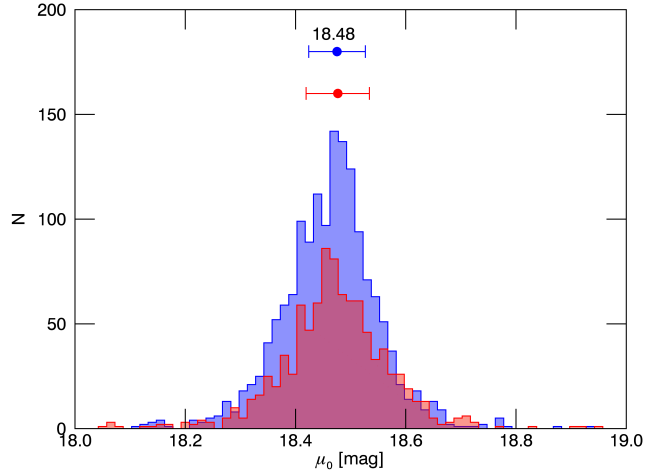


FIG. 14.— Histogram of the true distance moduli $\mu_{0,i}$ distribution for FU (blue bars) and FO Cepheids obtained from Equation 10. The blue dot indicates the median distance from the FU Cepheids' distribution, while the error bar indicates the 1σ dispersion around the median, $\sigma=0.10$ mag. The red dots shows the same for FO Cepheids, with $\sigma=0.11$ mag. We thus find a median distance modulus to the LMC $\mu=18.48 \pm 0.10$ mag for both FU and FO Cepheids. The above value is in excellent agreement with the mean distance modulus by P13, which is accurate to 2.2%.

the bins, where the error σ_{EVI} is given by the sum in quadrature of the error on $E(V - I)$ from H11(30–400%) and from our estimates (0.2–10%).

Moreover, our new reddening map has two significant advantages when compared to the map provided by H11: *a*) it covers a double area of the LMC (80 vs 40 square degrees), and in particular, it covers the whole disk for the very first time; *b*) it is characterised by a much higher accuracy. The total error (including systematics) on the reddening is smaller than 10%, which is one order of magnitude better than the typical accuracy of existing reddening maps.

To further quantify the accuracy of the current reddening estimates, we performed a detailed comparison with accurate reddening measurements available in the literature. Recently, P13 measured extinction for eight double eclipsing binary systems (DEBs) located in the bar and on the left arm of the LMC. We performed a beam search of $5'$ in radius around these systems and computed the median extinction from the Cepheids included in these radius. The comparison between the values based on Cepheids and the ones obtained by P13 is shown in Table 7. The reddening values are in excellent agreement for six out of the eight systems for which we found the match. In two cases (OGLE-LMC-ECL-26122, OGLE-LMC-ECL-09114), our reddening values are lower than the ones obtained by P13. However, on the basis of their individual distances these two systems seem to be located behind the plane of the LMC disk, and thus they might suffer a higher extinction when compared with Cepheids located in the LMC bar.

Marconi et al. (2013) find an extinction of $E(V - I) = 0.171 \pm 0.015$ mag for the Cepheid OGLE-LMC-CEP-0227, belonging to a detached double-lined eclipsing binary system located at $(\alpha, \delta)=(73^\circ.0654, -70^\circ.2420)$. We found a median extinction $E(V - I) = 0.157 \pm 0.001$ mag for the Cepheids at $5'$ in radius from this system, thus in perfect agreement with the value by Marconi et al.

(2013).

Recently, Elgueta et al. (2016) estimates the distance and reddening to the OGLE-LMC-ECL-25658 binary system, which is located at $(\alpha, \delta)=(90.4949, -68.5153)$. They found $E(B - V) = 0.091 \pm 0.030$ mag, while we found $E(B - V) = 0.096 \pm 0.005$ mag for a Cepheids located at $(\alpha, \delta)=(90.2155, -67.8089)$ and $E(B - V) = 0.105 \pm 0.005$ mag for a Cepheids located at $(\alpha, \delta)=(90.6012, -69.2539)$.

The comparison with literature values further supports the precision and the accuracy of the reddening map we estimated using classical Cepheids as tracers of stellar populations in the LMC disk.

7.2. Period-Luminosity relations corrected for reddening

The accurate individual reddening values we determined for all the Cepheids in our Sample B, allow us to determine new PL relations for the LMC Cepheids in six different bands. We adopted the following absorption coefficients for unit of $E(B - V)$: $A_I = 0.608, A_J = 0.292, A_H = 0.181, A_{K_S} = 0.119$ and $A_{w1} = 0.055$, to transform the $E(B - V)$ values into the absorption in each band. Thus, we computed the reddening-corrected magnitude for each Cepheid in each band and performed a least-squares fit to determine the PL relations in the form: $a + b \log P$. The best-fit parameters and dispersions of the six PL relations for FU and FO Cepheids are given in Table 8. Note that the slopes we find are in agreement within 1σ or better (see e.g. the J band PL) with the ones from theoretical predictions listed in Table 6. Moreover, we also list the PL relations obtained by adopting the extinction values by H11 for $\sim 1,120$ FU and ~ 780 Cepheids. The slopes found with the two different values of the reddening agree inside the error-bar given by the scatter of the relation. However, the dispersion around the optical PL relations obtained by using the H11 correction are a factor 1.5 (I) and 2.5 (V) larger than the ones found by using our new correction. This finding further supports the high accuracy of our new reddening map for the LMC disk. Moreover, the slopes of the J, H and K_S PL relations are in excellent agreement with the ones found by P04, who adopted the reddening computed for 51 Cepheids by Gieren et al. (1998), and with the ones by Storm et al. (2011b), who used instead a completely independent approach based on the Baade-Wesselink method. Finally, the new slopes are also in excellent agreement with the ones found by Macri et al. (2015) by adopting the reddening corrections by H11. In fact, the agreement is at 0.1σ level for our relations estimated by using the reddening corrections by H11, and at 1σ level when using our new reddening corrections.

8. SUMMARY AND DISCUSSION

We collected the largest ($\sim 4,000$) sample of optical-NIR-MIR measurements for LMC Cepheids. The use of multi-wavelength observations and of accurate NIR templates, allowed us to determine 3%(optical)–15%(NIR) precise individual distances for the entire sample of Cepheids. Moreover, we adopted theoretical predictions based on up-to-date pulsation models to quantify possible systematic errors on individual Cepheid distances.

We found that individual distances based on optical PW relations are more affected by systematics (uncer-

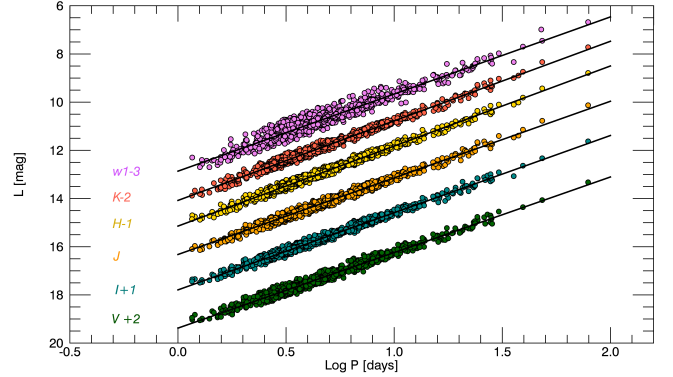


FIG. 15.— PL relations for FU Cepheids in our Sample B corrected for reddening by using our new reddening map. The best-fit parameters of the PL relations are given in Table 8. The dispersion around each of this relation ranges between 0.09 mag (V -band) to 0.17 mag ($w1$ -band), which is a factor 65%(V -band)–10(K_S -band)% smaller than the dispersion when no reddening correction is applied (see Table 8). The PL have been arbitrarily shifted in integer magnitude steps to improve the clarity of the figure (see annotations).

tainty on the adopted reddening law, intrinsic dispersion), when compared with distances based on NIR PW relations. Using the predicted intrinsic dispersion for the PW_{VI} relation (~ 0.06 mag), we found that individual distances *only* based on optical mean magnitudes cannot have an accuracy better than 7%. On the other hand, the simultaneous use of the three NIR bands: J, H and K_S , allow us to nail down the systematics and to provide individual distances with an accuracy better than 1.5%. However, the uncertainty on the W_{HJK} mean magnitudes due to the photometric errors ($\sigma_{J=17} \sim 0.05$ – 0.15 mag) on single observations effectively limits the above accuracy, for some samples, to 15%. The error budget on individual Cepheid distances, when moving from optical to NIR bands is dominated by different uncertainties (systematics vs measurement errors). This gives us the unique opportunity to internally validate distances together with their errors and reddening. Our main results are summarized in the following.

- *Viewing angles* – We find that the disk of the LMC is oriented with an inclination of $i = 25.05 \pm 0.02$ (stat.) ± 0.55 (syst.) deg and a position angle of $P.A. = 150.76 \pm 0.02$ (stat.) ± 0.07 (syst.). These values are in excellent agreement with recent estimates based on stellar tracers of similar age (RSG stars, van der Marel & Kallivayalil 2014). On the other hand, previous investigations based on Cepheids found larger inclinations (Nikolaev et al. 2004; Haschke et al. 2012, P04) and smaller position angles (Haschke et al. 2012, P04). The difference is caused by the different spatial distribution of the adopted Cepheid samples. The LMC viewing angles depend, due to its non-axisymmetric shape, on the sky coverage of the adopted stellar tracers. Moreover, the dependence of the inclination on the distance from the center of the distribution is mainly due to a limited mapping of the disk. Using Cepheids that are only located in the central fields, i.e., the LMC bar according to the definition by Nikolaev et al. (2004), we found $i = 35.^\circ 8 \pm 5^\circ$. Note that the error reported here and in the following is the difference between the angles found by adopting the PW_{VI} and the PW_{HJK} relations. If we extend the region covered by Cepheids towards the

western part, i.e., till the edge of the north-western arm, we found $i = 30^\circ \pm 10^\circ$, which is very close to the values found by Weinberg & Nikolaev (2001) and by Nikolaev et al. (2004).

If we exclude the Cepheids located across the bar, the inclination is $\sim 24^\circ.2$, thus perfectly consistent with what we have already found using the entire sample. This finding further supports the evidence that the current Cepheid sample allow us to precisely determine its geometry, since it traces the whole LMC disk, i.e., the bar plus the spiral arms. There is mounting empirical evidence that stellar tracers ranging from old, low-mass (RR Lyraes) to intermediate-mass (planetary nebulae, red clump, AGB) stars and evolved young massive stars (RSGs) do provide different viewing angles. The difference between old and young stellar tracers indicate that the former one is slightly less inclined by $\sim 3^\circ$ and has a position angle $\sim 20^\circ$ degree larger than those based on Cepheids. The above evidence needs to be supported by radial velocity measurements for large samples of the quoted stellar tracers.

A few years ago, Minniti et al. (2003) using accurate individual distances of 43 LMC RR Lyrae based on the K-band PL relations and kinematic measurements, proposed the possible existence of a dynamically hot spherical halo surrounding the LMC. However, subsequent estimates based on star counts covering a broader area up to 20° from the LMC center (Saha et al. 2010) and on RG kinematics (Gallart et al. 2004; Carrera et al. 2011) did not support this finding. The possible occurrence of an extended disk is also still controversial (Majewski et al. 2009; Saha et al. 2010; Besla et al. 2016). The same outcome applies to the possible occurrence of metallicity gradients among the individual stellar components. The possible occurrence of radial gradients in the metallicity distribution appears even more promising, since it will allow us to couple the different star formation events with their own chemical enrichments and their radial migrations. The MCs play in this context a crucial role, since the difference in radial distance among the different stellar tracers is negligible.

•*Distance to the LMC*– Taking advantage of the multi-band (optical-NIR-MIR) data-set, we adopted the reddening-law fitting method (Freedman et al. 1985) to determine simultaneously the true distance modulus and the reddening of the entire Cepheid sample. We take account for both estimate and systematic error on individual distance moduli and we found that the final error ranges from 0.1% to 0.7%. We computed the LMC distance distribution and we found that the median is $\mu_0 = 18.48 \pm 0.10$ mag using both fundamental and first overtone Cepheids. The above error, estimated as the standard deviation around the median, accounts for both statistical and systematic effects, but neglects the error on the zero-point of the photometric calibration (~ 0.02 mag). The excellent agreement on the distance based on fundamental and first overtone Cepheids further supports the use of FO Cepheids as solid distance indicators (Bono et al. 2010; Inno et al. 2013). Moreover, our estimate of the mean distance to the LMC is also in excellent agreement with similar estimates, but based on a smaller Cepheid sample (Inno et al. 2013), and with the geometrical distance obtained by Pietrzyński et al. (2013) on the basis of eclipsing binary systems.

•*Reddening towards the LMC disk* – The reddening-law fitting method provides individual reddening estimates for each Cepheid in our sample, with an accuracy better than 20%. We compared the current reddening values with those available in the literature and we found that the current reddening map agrees quite well with the one provided by Haschke et al. (2011) using RC stars, but it is one order of magnitude more accurate and a factor of two larger. We provide the entire Cepheid catalog with mean NIR and MIR magnitudes, together with the individual distances and extinction values.

We demonstrated that the use of NIR PW relations to determine Cepheids individual distances is extremely promising. However, NIR surveys towards the LMC with modest photometric precision ($\sigma_{J=17} \sim 0.05\text{--}0.15$ mag, on single observations) do not allow us to fully exploit the intrinsic accuracy of NIR distance diagnostics. However, accurate NIR templates allow us to use highly-accurate single-epoch photometric measurements available in the literature to match the precision typical of distance determinations based on optical bands.

The current approach based on measurements ranging from optical to mid-infrared observations of classical Cepheids, appears very promising for accurate individual distance determinations and paves the way to accurate estimates of their intrinsic properties as a function of the radial distribution.

We will complement the accurate information on the three-dimensional distribution presented here with individual radial velocities and chemical abundances for a significant fraction of the Cepheids in our sample. The kinematic and the chemical tagging of a significant fraction of LMC Cepheids will allow us to further constrain the physical properties of the young stellar population in the LMC disk.

This work was supported by Sonderforschungsbereich SFB 881 "The Milky Way System" (subproject C9) of the German Research Foundation (DFG). The OGLE project has received funding from the National Science Centre, Poland, grant MAESTRO 2014/14/A/ST9/00121 to AU. One of us (G.B.) thanks the Japan Society for the Promotion of Science for a research grant (L15518). It is also a pleasure to thank the anonymous referee for his/her supportive attitude and insightful suggestions that helped us to improve the readability of the paper.

REFERENCES

- Alcock, C., Allsman, R. A., Alves, D. R., et al. 2000, *ApJ*, 542, 281
- Benedict, G. F., McArthur, B. E., Feast, M. W., et al. 2007, *AJ*, 133, 1810
- Besla, G., Kallivayalil, N., Hernquist, L., et al. 2012, *MNRAS*, 421, 2109
- Bono, G., Genovali, K., Lemasle, B., et al. 2015, Fifty Years of Wide Field Studies in the Southern Hemisphere: Resolved Stellar Populations of the Galactic Bulge and Magellanic Clouds, 491, 148
- Bono, G., Caputo, F., Marconi, M., & Musella, I. 2010, *ApJ*, 715, 277
- Bono, G., Groenewegen, M. A. T., Marconi, M., & Caputo, F. 2002, *ApJ*, 574, L33
- Bono, G., Castellani, V., & Marconi, M. 2000, *ApJ*, 529, 293
- Bono, G., Marconi, M., & Stellingwerf, R. F. 1999, *ApJS*, 122, 167
- Bono, G., Caputo, F., Castellani, V., & Marconi, M. 1999, *ApJ*, 512, 711
- Besla, G., Kallivayalil, N., Hernquist, L., et al. 2007, *ApJ*, 668, 949
- Besla, G., Martinez-Delgado, D., van der Marel, R. P., et al. 2016, *arXiv:1602.04222*
- Cardelli, J. A., Clayton, G. C., & Mathis, J. S. 1989, *Interstellar Dust*, 135, 5
- Carrera, R., Gallart, C., Aparicio, A., & Hardy, E. 2011, *AJ*, 142, 61
- Casetti-Dinescu, D. I., Moni Bidin, C., Girard, T. M., et al. 2014, *ApJ*, 784, L37
- Carpenter, J. M. 2001, *AJ*, 121, 2851
- Cioni, M.-R. L., van der Marel, R. P., Loup, C., & Habing, H. J. 2000, *A&A*, 359, 601
- Cioni, M.-R. L., Clementini, G., Girardi, L., et al. 2011, *A&A*, 527, A116
- Clementini, G., Gratton, R. G., Bragaglia, A., et al. 2000, *arXiv:astro-ph/0007471*
- Cutri, R. M., Wright, E. L., Conrow, T., et al. 2013, Explanatory Supplement to the AllWISE Data Release Products, by R. M. Cutri et al. ,
- Deb, S., & Singh, H. P. 2014, *MNRAS*, 438, 2440
- Diaz, J. D., & Bekki, K. 2012, *ApJ*, 750, 36
- Diaz, J., & Bekki, K. 2011, *MNRAS*, 413, 2015
- De Marchi, G., Panagia, N., Sabbi, E., et al. 2016, *MNRAS*, 455, 4373
- de Vaucouleurs, G., & Freeman, K. C. 1972, *Vistas in Astronomy*, 14, 163
- D’Onghia, E., & Fox, A. J. 2015, *arXiv:1511.05853*
- Elgueta, S. S., Graczyk, D., Gieren, W., et al. 2016, *arXiv:1605.00909*
- Epchtein, N. 1998, *New Horizons from Multi-Wavelength Sky Surveys*, 179, 106
- Fabrizio, M., Nonino, M., Bono, G., et al. 2015, *A&A*, 580, A18
- Fabrizio, M., Nonino, M., Bono, G., et al. 2011, *PASP*, 123, 384
- Fiorentino, G., Musella, I., & Marconi, M. 2013, *MNRAS*, 434, 2866
- Freedman, W. L., Grieve, G. R., & Madore, B. F. 1985, *ApJS*, 59, 311
- Freedman, W. L. 1988, *ApJ*, 326, 691
- Freedman, W. L., Wilson, C. D., & Madore, B. F. 1991, *ApJ*, 372, 455
- Fouqué, P., Arriagada, P., Storm, J., et al. 2007, *A&A*, 476, 73
- Gallart, C., Stetson, P. B., Hardy, E., Pont, F., & Zinn, R. 2004, *ApJ*, 614, L109
- Gieren, W. P., Fouqué, P., & Gómez, M. 1998, *ApJ*, 496, 17
- Haschke, R., Grebel, E. K., & Duffau, S. 2011, *AJ*, 141, 158
- Haschke, R., Grebel, E. K., & Duffau, S. 2012, *AJ*, 144, 106
- Kato, D., Nagashima, C., Nagayama, T., et al. 2007, *PASJ*, 59, 615
- Kallivayalil, N., van der Marel, R. P., Besla, G., Anderson, J., & Alcock, C. 2013, *ApJ*, 764, 161
- Kim, S., Staveley-Smith, L., Dopita, M. A., et al. 1998, *ApJ*, 503, 674
- Koen, C., Kanbur, S., & Ngeow, C. 2007, *MNRAS*, 380, 1440
- Indu, G., & Subramaniam, A. 2015, *A&A*, 573, A136
- Inno, L., Matsunaga, N., Bono, G., et al. 2013, *ApJ*, 764, 84
- Inno, L., Matsunaga, N., Romaniello, M., et al. 2015, *A&A*, 576, A30
- Jacyszyn-Dobrzaniecka, A. M., Skowron, D. M., Mróz, P., et al. 2016, *Acta Astron.*, 66, 149
- Macri, L. M., Ngeow, C.-C., Kanbur, S. M., Mahzooni, S., & Smitka, M. T. 2015, *AJ*, 149, 117
- Majewski, S. R., Nidever, D. L., Muñoz, R. R., et al. 2009, *The Magellanic System: Stars, Gas, and Galaxies*, 256, 51
- Marengo, M., Evans, N. R., Barmby, P., et al. 2010, *ApJ*, 709, 120
- Marconi, M., Musella, I., & Fiorentino, G. 2005, *ApJ*, 632, 590
- Marconi, M., Molinaro, R., Bono, G., et al. 2013, *ApJ*, 768, L6
- Mathewson, D. S., Cleary, M. N., & Murray, J. D. 1974, *ApJ*, 190, 291
- McCall, M. L. 2004, *AJ*, 128, 2144
- Minniti, D., Borissova, J., Rejkuba, M., et al. 2003, *Science*, 301, 1508
- Monelli, M., Pulone, L., Corsi, C. E., et al. 2003, *AJ*, 126, 218
- Nikolaev, S., Drake, A. J., Keller, S. C., et al. 2004, *ApJ*, 601, 260
- Ngeow, C.-C., Marconi, M., Musella, I., Cignoni, M., & Kanbur, S. M. 2012, *ApJ*, 745, 104
- Olsen, K. A. G., Zaritsky, D., Blum, R. D., Boyer, M. L., & Gordon, K. D. 2011, *ApJ*, 737, 29
- Persson, S. E., Madore, B. F., Krzemiński, W., et al. 2004, *AJ*, 128, 2239 (P04)
- Pietrzyński, G., Graczyk, D., Gieren, W., et al. 2013, *Nature*, 495, 76
- Rich, J. A., Persson, S. E., Freedman, W. L., et al. 2014, *ApJ*, 794, 107
- Ripepi, V., Moretti, M. I., Marconi, M., et al. 2012, *MNRAS*, 424, 1807
- Romaniello, M., Primas, F., Mottini, M., et al. 2008, *A&A*, 488, 731
- Rubele, S., Kerber, L., Girardi, L., et al. 2012, *A&A*, 537, A106
- Saha, A., Olszewski, E. W., Brondel, B., et al. 2010, *AJ*, 140, 1719
- Skrutskie, M. F., Cutri, R. M., Stiening, R., et al. 2006, *AJ*, 131, 1163
- Soszyński, I., Gieren, W., & Pietrzyński, G. 2005, *PASP*, 117, 823
- Soszyński, I., Poleski, R., Udalski, A., et al. 2008, *Acta Astron.*, 58, 163
- Soszyński, I., Udalski, A., Szymański, M. K., et al. 2015, *Acta Astron.*, 65, 297
- Storm, J., Gieren, W., Fouqué, P., et al. 2011, *A&A*, 534, A95 (S11a)
- Storm, J., Gieren, W., Fouqué, P., et al. 2011, *A&A*, 534, A95 (S11b)
- Subramanian, S., & Subramaniam, A. 2013, *A&A*, 552, A144
- van der Marel, R. P., & Cioni, M.-R. L. 2001, *AJ*, 122, 1807
- van der Marel, R. P. 2001, *AJ*, 122, 1827
- van der Marel, R. P., & Kallivayalil, N. 2014, *ApJ*, 781, 121
- van Leeuwen, F., Feast, M. W., Whitelock, P. A., & Laney, C. D. 2007, *MNRAS*, 379, 723
- Weinberg, M. D., & Nikolaev, S. 2001, *ApJ*, 548, 712

TABLE 1
SUB-SAMPLES ADOPTED

SAMPLE	FU #	FU Period range [days]	FO #	FO Period range [days]	Use of the Templates	$\sigma_{Ph}@ J=16$ mag [mag]
VMC	142	1–20.1	118	0.7–5	Y	0.03
IRSF	1418	1–28.8	846	0.7–6	Y	0.03
CPAPIER	60	1–28.2	48	0.7–5	Y	0.10
2MASS	560	1–28.0	525	0.7–5	Y	0.10
P04	65	2–99.2	–	–	N	0.02
WISE	1,557	2–63	1,086	0.7–5	N	0.02
TOTAL Sample A ^a	2,245	1–99.2	1,537	0.7–6		
TOTAL Sample B ^b	1,557	1–99.2	1,086	0.7–6		

^a optical-NIR dataset

^b optical-NIR-MIR dataset

TABLE 2
THEORETICAL NIR AND OPTICAL-NIR PW RELATIONS FOR LMC CEPHEIDS IN
THE FORM: $a + b \log P$

Wesenheit definition	$a \pm \sigma_a$	$b \pm \sigma_b$	σ
$W_{JH} = H - 1.63 \times (J - H)$	-3.066 ± 0.002	-3.464 ± 0.002	0.011 ^b
$W_{HJK} = H - 1.046 \times (J - K_S)$	-2.930 ± 0.001	-3.394 ± 0.001	0.027
$W_{JK} = K_S - 0.69 \times (J - K_S)$	-2.849 ± 0.001	-3.351 ± 0.001	0.038
$W_{IH} = H - 0.42 \times (I - H)$	-2.869 ± 0.001	-3.348 ± 0.001	0.038
$W_{HIK} = H - 0.370 \times (I - K_S)$	-2.849 ± 0.001	-3.338 ± 0.001	0.041
$W_{VH} = H - 0.22 \times (V - H)$	-2.866 ± 0.001	-3.339 ± 0.001	0.041
$W_{HVI} = H - 0.461 \times (V - I)$	-2.862 ± 0.001	-3.330 ± 0.001	0.044
$W_{KIH} = K_S - 0.279 \times (I - H)$	-2.809 ± 0.001	-3.321 ± 0.001	0.045
$W_{KVH} = K_S - 0.145 \times (V - H)$	-2.805 ± 0.001	-3.315 ± 0.001	0.047
$W_{IK} = K_S - 0.24 \times (I - K_S)$	-2.791 ± 0.001	-3.314 ± 0.001	0.047
$W_{VK} = K_S - 0.13 \times (V - K_S)$	-2.792 ± 0.001	-3.309 ± 0.001	0.049
$W_{KVI} = K_S - 0.304 \times (V - I)$	-2.778 ± 0.001	-3.285 ± 0.001	0.053
$W_{JIH} = J - 0.684 \times (I - H)$	-2.753 ± 0.001	-3.278 ± 0.001	0.055
$W_{VI} = I - 1.55 \times (V - I)$	-2.838 ± 0.002	-3.286 ± 0.002	0.058
$W_{HK} = K_S - 1.92 \times (H - K_S)$	-2.689 ± 0.002	-3.268 ± 0.002	0.059
$W_{JVK} = J - 0.331 \times (V - K_S)$	-2.724 ± 0.001	-3.255 ± 0.001	0.062
$W_{JVI} = J - 0.745 \times (V - I)$	-2.737 ± 0.001	-3.248 ± 0.001	0.065
$W_{VJ} = J - 0.41 \times (V - J)$	-2.693 ± 0.001	-3.231 ± 0.001	0.068
$W_{IJ} = J - 0.92 \times (I - J)$	-2.642 ± 0.001	-3.212 ± 0.001	0.072
$W_{HVK} = H - 1.135 \times (V - K_S)$	-3.939 ± 0.001	-3.942 ± 0.001	0.092

^a

^a

^a The PW relations are listed in order of ascending dispersion

^b The PW_{JH} relation shows the smallest intrinsic dispersion. However, we did not adopt this relation because of the coefficient significantly larger than 1 ($\frac{AH}{E(J-H)}=1.63$) in the Wesenheit definition. In fact, the photometric error on the mean color $E(J-H)$ is also multiplied by the same factor, resulting on larger errors on the final Wesenheit magnitude.

TABLE 3
OBSERVED NIR AND OPTICAL-NIR PW RELATIONS FOR LMC CEPHEIDS IN THE
FORM: $a + b \log P$

Wesenheit definition	$a \pm \sigma_a$	$b \pm \sigma_b$	Num	σ
FU CEPHEIDS				
$W_{JH} = H - 1.63 \times (J - H)$	15.677 ± 0.003	-3.377 ± 0.005	2159	0.12
$W_{HJK} = H - 1.046 \times (J - K_S)$	15.788 ± 0.003	-3.357 ± 0.004	2164	0.10
$W_{JK} = K_S - 0.69 \times (J - K_S)$	15.846 ± 0.002	-3.331 ± 0.003	2149	0.11
$W_{IH} = H - 0.42 \times (I - H)$	15.831 ± 0.002	-3.334 ± 0.003	2168	0.09
$W_{HIK} = H - 0.370 \times (I - K_S)$	15.849 ± 0.002	-3.335 ± 0.003	2173	0.09
$W_{VH} = H - 0.22 \times (V - H)$	15.837 ± 0.002	-3.331 ± 0.002	2168	0.09
$W_{HVI} = H - 0.461 \times (V - I)$	15.847 ± 0.002	-3.330 ± 0.002	2170	0.08
$W_{KIH} = K_S - 0.279 \times (I - H)$	15.876 ± 0.002	-3.321 ± 0.003	2161	0.09
$W_{KVH} = K_S - 0.145 \times (V - H)$	15.881 ± 0.002	-3.318 ± 0.003	2166	0.09
$W_{IK} = K_S - 0.24 \times (I - K_S)$	15.887 ± 0.002	-3.312 ± 0.003	2164	0.09
$W_{VK} = K_S - 0.13 \times (V - K_S)$	15.894 ± 0.002	-3.314 ± 0.002	2170	0.09
$W_{KVI} = K_S - 0.304 \times (V - I)$	15.944 ± 0.002	-3.291 ± 0.002	2173	0.09
$W_{JIH} = J - 0.684 \times (I - H)$	15.917 ± 0.002	-3.305 ± 0.003	2175	0.10
$W_{VI} = I - 1.55 \times (V - I)$	15.897 ± 0.001	-3.327 ± 0.001	2168	0.08
$W_{HK} = K_S - 1.92 \times (H - K_S)$	15.979 ± 0.004	-3.308 ± 0.005	2114	0.15
$W_{JVK} = J - 0.331 \times (V - K_S)$	15.947 ± 0.002	-3.294 ± 0.003	2169	0.09
$W_{JVI} = J - 0.745 \times (V - I)$	15.948 ± 0.001	-3.299 ± 0.001	2175	0.08
$W_{VJ} = J - 0.41 \times (V - J)$	15.971 ± 0.002	-3.284 ± 0.002	2172	0.10
$W_{IJ} = J - 0.92 \times (I - J)$	15.997 ± 0.002	-3.269 ± 0.003	2168	0.11
$W_{HVK} = H - 1.135 \times (V - K_S)$	14.537 ± 0.003	-3.813 ± 0.004	2147	0.19
$W_{Jw1} = w1 - 0.23 \times (J - w1)$	15.756 ± 0.007	-3.199 ± 0.008	1489	0.20
$W_{Hw1} = w1 - 0.43 \times (H - w1)$	15.767 ± 0.007	-3.167 ± 0.008	1489	0.23
$W_{Kw1} = w1 - 0.86 \times (K_S - w1)$	15.708 ± 0.007	-3.123 ± 0.008	1483	0.29
$W_{Iw1} = w1 - 0.10 \times (I - w1)$	15.791 ± 0.007	-3.217 ± 0.008	1486	0.18
$W_{Vw1} = w1 - 0.06 \times (V - w1)$	15.792 ± 0.007	-3.218 ± 0.008	1488	0.18
FO CEPHEIDS				
$W_{JH} = H - 1.63 \times (J - H)$	15.176 ± 0.004	-3.458 ± 0.011	1505	0.15
$W_{HJK} = H - 1.046 \times (J - K_S)$	15.258 ± 0.004	-3.382 ± 0.010	1539	0.14
$W_{JK} = K_S - 0.69 \times (J - K_S)$	15.305 ± 0.003	-3.323 ± 0.007	1526	0.16
$W_{IH} = H - 0.42 \times (I - H)$	15.316 ± 0.003	-3.430 ± 0.007	1543	0.13
$W_{HIK} = H - 0.370 \times (I - K_S)$	15.328 ± 0.003	-3.418 ± 0.008	1534	0.12
$W_{VH} = H - 0.22 \times (V - H)$	15.328 ± 0.002	-3.438 ± 0.006	1544	0.12
$W_{HVI} = H - 0.461 \times (V - I)$	15.340 ± 0.002	-3.440 ± 0.006	1544	0.10
$W_{KIH} = K_S - 0.279 \times (I - H)$	15.343 ± 0.003	-3.363 ± 0.007	1524	0.13
$W_{KVH} = K_S - 0.145 \times (V - H)$	15.350 ± 0.003	-3.362 ± 0.007	1524	0.13
$W_{IK} = K_S - 0.24 \times (I - K_S)$	15.358 ± 0.002	-3.357 ± 0.006	1522	0.14
$W_{VK} = K_S - 0.13 \times (V - K_S)$	15.364 ± 0.002	-3.358 ± 0.006	1521	0.13
$W_{KVI} = K_S - 0.304 \times (V - I)$	15.440 ± 0.002	-3.421 ± 0.006	1549	0.11
$W_{JIH} = J - 0.684 \times (I - H)$	15.402 ± 0.002	-3.427 ± 0.006	1562	0.14
$W_{VI} = I - 1.55 \times (V - I)$	15.394 ± 0.001	-3.434 ± 0.001	1554	0.08
$W_{HK} = K_S - 1.92 \times (H - K_S)$	15.421 ± 0.006	-3.281 ± 0.015	1513	0.24
$W_{JVK} = J - 0.331 \times (V - K_S)$	15.426 ± 0.002	-3.400 ± 0.005	1558	0.12
$W_{JVI} = J - 0.745 \times (V - I)$	15.438 ± 0.001	-3.427 ± 0.004	1566	0.11
$W_{VJ} = J - 0.41 \times (V - J)$	15.458 ± 0.002	-3.416 ± 0.004	1565	0.13
$W_{IJ} = J - 0.92 \times (I - J)$	15.478 ± 0.002	-3.402 ± 0.005	1568	0.16
$W_{HVK} = H - 1.135 \times (V - K_S)$	13.948 ± 0.004	-3.503 ± 0.010	1543	0.25
$W_{Jw1} = w1 - 0.23 \times (J - w1)$	15.253 ± 0.003	-3.331 ± 0.007	1036	0.22
$W_{Hw1} = w1 - 0.43 \times (H - w1)$	15.293 ± 0.006	-3.240 ± 0.014	1039	0.26
$W_{Kw1} = w1 - 0.86 \times (K_S - w1)$	15.212 ± 0.004	-3.320 ± 0.010	1038	0.34
$W_{Iw1} = w1 - 0.10 \times (I - w1)$	15.250 ± 0.001	-3.319 ± 0.003	1038	0.20
$W_{Vw1} = w1 - 0.06 \times (V - w1)$	15.252 ± 0.001	-3.318 ± 0.003	1037	0.19

TABLE 4
LIST OF THE VALUES ADOPTED AS THE CENTER OF THE DISTRIBUTION FOR LMC CEPHEIDS

Definition	α_0 [ddeg]	δ_0 [ddeg]	Reference	ID
Cepheids centroid	80.78	-69.30	This work	CI
HI rotation center	79.40	-69.03	Kim et al. (1998)	CII
optical center	79.91	-69.45	de Vaucouleurs & Freeman (1972)	CIII
Cepheids geometrical center	80.40	-69.00	Nikolaev et al. (2004)	CIV
NIR isophote center	81.28	-69.78	van der Marel (2001)	CV

TABLE 5
 INCLINATION AND POSITION ANGLE FOR THE LMC

Tracers	P.A. [ddeg]	i [ddeg]	Reference	Adopted Center (ID)	sky coverage [deg × deg]
Cepheids, PW _{VI}	150.72 ± 0.02	24.46 ± 0.01	This work	CI	11.2×14
FU Cepheids, PW _{VI}	150.79 ± 0.03	24.22 ± 0.01	This work	CI	11×11
FO Cepheids, PW _{VI}	150.68 ± 0.03	24.58 ± 0.02	This work	CI	11.2×14
Cepheids, PW _{VI}	151.89 ± 0.02	24.57 ± 0.01	This work	CII	11.2×14
Cepheids, PW _{VI}	151.53 ± 0.02	24.60 ± 0.01	This work	CIII	11.2×14
Cepheids, PW _{VI}	151.32 ± 0.02	24.56 ± 0.01	This work	CIV	11.2×14
Cepheids, PW _{VI}	150.38 ± 0.02	24.62 ± 0.01	This work	CV	11.2×14
Cepheids, PW _{HJK}	150.79 ± 0.02	25.56 ± 0.01	This work	CI	11.2×14
FU Cepheids, PW _{HJK}	150.77 ± 0.03	23.42 ± 0.02	This work	CI	11×11
FO Cepheids, PW _{HJK}	150.67 ± 0.03	27.54 ± 0.02	This work	CI	11.2×14
Cepheids, PW _{HJK}	150.60 ± 0.02	25.16 ± 0.02	This work	CII	11.2×14
Cepheids, PW _{HJK}	151.61 ± 0.02	25.07 ± 0.02	This work	CIII	11.2×14
Cepheids, PW _{HJK}	150.26 ± 0.02	25.46 ± 0.02	This work	CIV	11.2×14
Cepheids, PW _{HJK}	151.95 ± 0.02	25.41 ± 0.02	This work	CV	11.2×14
Cepheids, best value	150.76 ± 0.02 ± 0.07	25.05 ± 0.02 ± 0.55	This work	CI	11.2×14
Cepheids, PW _{VI}	151.4 ± 1.5	24.2 ± 0.6	Jacyszyn-Dobrzniecka et al. (2016)	CII	11.2×14
Cepheids, PL(V,I)	116 ± 18	32 ± 4	Haschke et al. (2012)	CV	8×6.5
Cepheids, PL(V,R,J,H,K)	150.2 ± 2.4	31 ± 1	Nikolaev et al. (2004)	CIV	8×7
Cepheids, PL(J,H,K)	127 ± 10	27 ± 6	P04	...	6.5×6.5
RSG ^a , 3D-kinematics	154.5 ± 2.1	26.2 ± 5.9	van der Marel & Kallivayalil (2014)	CII	6.5×8
AGB ^b , kinematics	122.5 ± 8.3	34.7 ± 6.2	van der Marel (2001)	CV	...
AGB ^b , kinematics	142 ± 5	...	Olsen et al. (2011)	CIII	8×4
RC	148.3 ± 3.8	26.6 ± 1.3	Subramanian & Subramaniam (2013)	CIII	8×6.5
RGs	122 ± 8	...	Cioni et al. (2000)	CV	19.9×16
RGs ^c , 3D-kinematics	139.1 ± 4.1	34.0 ± 7.0	van der Marel & Kallivayalil (2014)	CII	6.5×8
RRab Lyrae	175.22 ± 0.01	22.25 ± 0.01	Deb & Singh (2014)	CIII	8×5
HI	168 ± 1	22 ± 6	Kim et al. (1998)	CII	8×4
HI	126 ± 23	...	Indu & Subramaniam (2015)	CII	20×20
Isophotes	170 ± 5	27 ± 2	de Vaucouleurs & Freeman (1972)	CIII	16×17

^a Red supergiant stars, typical ages ~10–50 Myr

^b Asymptotic giant branch stars, typical ages of ~100 Myr – 10 Gyr

^c Red giants, typical ages of ~1–12 Gyr

TABLE 6
 PL THEORETICAL RELATIONS FOR LMC CEPHEIDS IN
 THE FORM: $a + b \log P$

Band	$a \pm \sigma_a$	$b \pm \sigma_b$	σ
<i>V</i>	-1.447 ± 0.0004	-2.605 ± 0.0004	0.203
<i>I</i>	-1.987 ± 0.0004	-2.879 ± 0.0004	0.145
<i>J</i>	-2.324 ± 0.0004	-3.057 ± 0.0004	0.105
<i>H</i>	-2.610 ± 0.0004	-3.207 ± 0.0004	0.070
K_S	-2.636 ± 0.0004	-3.229 ± 0.0004	0.066

TABLE 7
COMPARISON OF REDDENING VALUES FROM DETACHED ECLIPSING BINARY SYSTEMS (DEBS) BY PIETRZYŃSKI ET AL. (2013) AND VALUES FROM OUR NEW REDDENING MAP.

DES Name	Ra [ddeg]	Dec [ddeg]	$E(B - V)_{DEBs}$ [mag]	$E(B - V)_{CEP}$ [mag]
OGLE-LMC-ECL-10567	78.50788	-68.6884	0.10 ± 0.02	0.11 ± 0.02
OGLE-LMC-ECL-26122	78.52520	-69.2658	0.14 ± 0.02	0.10 ± 0.01
OGLE-LMC-ECL-09114	77.58180	-68.9701	0.16 ± 0.02	0.10 ± 0.02
OGLE-LMC-ECL-06575	76.13696	-69.3475	0.11 ± 0.02	0.11 ± 0.02
OGLE-LMC-ECL-01866	73.06367	-68.3195	0.12 ± 0.02	0.10 ± 0.01
OGLE-LMC-ECL-03160	73.96450	-68.6633	0.12 ± 0.02	0.12 ± 0.02
OGLE-LMC-ECL-15260	81.35692	-69.5513	0.10 ± 0.02	0.08 ± 0.03

TABLE 8
OPTICAL, NIR AND MIR PL RELATIONS FOR LMC CEPHEIDS
CORRECTED FOR REDDENING

Wesenheit definition	$a \pm \sigma_a$	$b \pm \sigma_b$	Num	σ
FU CEPHEIDS				
V^a	17.172 ± 0.001	-2.807 ± 0.001	1526	0.08
I^a	16.674 ± 0.001	-3.017 ± 0.001	1520	0.08
J^a	16.256 ± 0.001	-3.068 ± 0.002	1516	0.09
H^a	16.102 ± 0.002	-3.257 ± 0.003	1514	0.08
K_S^a	16.053 ± 0.002	-3.261 ± 0.003	1518	0.09
$W1^a$	15.864 ± 0.006	-3.194 ± 0.007	1493	0.17
V^b	17.272 ± 0.002	-2.722 ± 0.003	1118	0.18
I^b	16.740 ± 0.002	-2.963 ± 0.003	1112	0.13
J^b	16.314 ± 0.001	-3.088 ± 0.002	1121	0.11
H^b	16.111 ± 0.002	-3.227 ± 0.003	1129	0.09
K_S^b	16.069 ± 0.002	-3.245 ± 0.003	1134	0.09
V^c	17.435 ± 0.002	-2.672 ± 0.002	1523	0.23
I^c	16.820 ± 0.002	-2.909 ± 0.002	1516	0.15
J^c	16.341 ± 0.001	-3.001 ± 0.002	1520	0.12
H^c	16.163 ± 0.002	-3.244 ± 0.003	1520	0.10
K_S^c	16.097 ± 0.002	-3.249 ± 0.003	1526	0.10
$w1^c$	15.853 ± 0.006	-3.156 ± 0.007	1498	0.18
FO CEPHEIDS				
V^a	16.789 ± 0.001	-3.080 ± 0.003	1056	0.09
I^a	16.234 ± 0.001	-3.201 ± 0.003	1063	0.09
J^a	15.842 ± 0.002	-3.312 ± 0.005	1067	0.11
H^a	15.512 ± 0.006	-3.265 ± 0.01	1059	0.11
K_S^a	15.535 ± 0.003	-3.330 ± 0.008	1035	0.12
$W1^a$	15.302 ± 0.001	-3.210 ± 0.003	1038	0.19
V^b	16.860 ± 0.001	-3.299 ± 0.004	795	0.19
I^b	16.285 ± 0.001	-3.334 ± 0.004	797	0.14
J^b	15.878 ± 0.002	-3.389 ± 0.005	797	0.12
H^b	15.626 ± 0.005	-3.455 ± 0.01	790	0.10
K_S^b	15.587 ± 0.003	-3.455 ± 0.007	788	0.10
V^c	16.963 ± 0.001	-3.141 ± 0.003	930	0.23
I^c	16.344 ± 0.001	-3.240 ± 0.003	931	0.16
J^c	15.914 ± 0.002	-3.334 ± 0.005	930	0.13
H^c	15.533 ± 0.006	-3.246 ± 0.01	928	0.12
K_S^c	15.567 ± 0.004	-3.336 ± 0.009	910	0.13
$w1^c$	15.383 ± 0.001	-3.322 ± 0.004	897	0.19

^a Reddening correction performed by adopting our estimates of $E(B - V)$

^b Reddening correction performed by adopting $E(V - I)$ taken from H11

^c No reddening correction performed

TABLE 9
EXAMPLE LINE OF THE PUBLISHED ONLINE CATALOG (COL. 1-12)

ID ^a	Mode	Sample ^b	Period	I^c	V^c	J^c	σ_J^d	H^c	σ_H^d	K_s^c	$\sigma_{K_s}^d$
HV6098	FU	P04	24.238	12.27	12.95	11.717	0.017	11.395	0.016	11.303	0.014

^a Name of the star: the the Harvard Variable catalog ID for the first ten Cepheids, and the OGLE ID for all the others in the OGLE catalog.

^b The sub-sample to which the Cepheid belongs, as defined in Table 1.

^c The mean intensity transformed into magnitude.

^d Error on the mean intensity transformed into magnitude.

TABLE 9
(CONT.) EXAMPLE LINE OF THE PUBLISHED ONLINE CATALOG (COL. 13-23)

α	δ	$w1$	σ_{w1}	$w1_{flag}^e$	$w1_{Nobs}^f$	DM ^g	σ_{DM}	$E(B - V)^h$	σ_E	χ^2_j
74.437668	-65.708359	11.247	0.035	Y	95	18.01	0.03	0.059	0.029	48

^e A flag that specifies if the $w1$ -band mean magnitude was obtained by performing the Fourier-fit (Flag = Y) or by adopting the error-weighted mean of the observed magnitudes (Flag = N).

^f Number of epochs available in the $w1$ band.

^g Distance modulus (in magnitude) obtained by adopting the reddening-fit method.

^h Color excess (in magnitude) obtained by adopting the reddening-fit method.

^j The χ^2 of the reddening-law fit.